An Investigation of Repulsive Capillary Forces

Name:	Rachid Hahury	Research institute:	ARCNL
Student number:	14100630	Project leader:	Steve Franklin
Course:	Graduation Internship	Supervisor:	Chen Xiao
Internship coach:	Bart Kieviet	Date:	03-09-2021

Acknowledgment

Throughout my graduation internship at ARCNL I received a great deal of support from several people, and I would like to thank them for their indispensable contribution to the result of this thesis.

First, I would like to thank my project leader, Professor Steve Franklin, for his guidance and support made sure this research was continually guided in the right direction. Next, I would like to thank my supervisor, dr. Chen Xiao, whose knowledge and insight was essential for the realization of this thesis. Thanks to their constructive feedback, I have learned to better evaluate my work, which has made me look more critically at the substantive aspects of my work, as well as helping me improve my qualities as a researcher.

Furthermore, I would like to thank dr. Felix Cassin, for his expertise on operating the Innova proved to be vital to the ramping experiment. I would also like to thank Jan Mathijssen and Zuedi Mazzota for helping me conduct the laser ablation experiment. Moreover, I want to thank all the other colleagues at ARCNL who were very kind and helpful and made me feel right at home.

It has been difficult times, not only during my internship but for the past couple of years in general. I would therefore like to thank my friends and family who have supported me throughout the years. Finally, I want to give special thanks to my grandfather, Ben Steen. His support, caring, and advice made it possible for me to be in the position where I am right now. Thank you sincerely.

Abstract

In ambient conditions, capillary condensation allows for the formation of capillary bridges. Since most surfaces are naturally hydrophilic, the capillary bridges result in an attractive capillary force, increasing the normal load. When two hydrophilic surfaces slide against each other, the attractive capillary force can negatively affect their friction and wear behavior. In this work, the mechanics and effects of repulsive capillary forces are investigated. On the theoretical side, a mathematical model for the case of a capillary bridge between two planar solids with equal contact angles has been developed. The model can be used to calculate the capillary forces given the volume of the capillary bridge, the contact angle, and the separation distance between the two surfaces. For a microscopic water droplet, repulsive forces in the order of 1 N, and stiffness values in the order of 10^8 $N \cdot m^{-1}$ can be expected. On the experimental side, a procedure has been established for the coating of silicon wafers and silicon dioxide colloidal probes with octyltrichlorosilane, rendering the surfaces hydrophobic. The contact angle of water on the coated silicon wafer is measured at (106±1)°, which is in agreement with the literature. Moreover, atomic force microscopy has been employed to measure the adhesion force between modified colloidal probes and silicon wafers. A reduction in the adhesion force of 68 to 90% is observed for a hydrophobic probe and wafer compared to a hydrophilic probe and wafer. In addition, the friction force has been measured between a combination of hydrophilic and hydrophobic wafers using a tribometer. For two hydrophilic wafers, the strong attractive capillary force resulted in a significant friction force. For two hydrophobic wafers, however, a 99% decrease in friction is observed, which can be attributed to the repulsive capillary force caused by the capillary bridges.

Table of contents

Nomenclature

Roman symbols

a	Distance between two objects [m]
A	Surface area [m^2]
A_H	Hamaker constant [J]
C	London coefficient [J]
D_C	Critical separation distance [m]
E	Energy [J]
F_{adh}	Adhesion force [N]
F_B	Chemical bonding force [N]
F_{cap}	Capillary force [N]
F_{el}	Electrostatic force [N]
F_F	Friction force [N]
F_{Lap}	Laplace force [N]
F_N	Normal force [N]
F_p	Pull-off force [N]
F_{ten}	Tension force [N]
F_{vdW}	Van der Waals force [N]
f_1, f_2	Fractional surface area of solid and liquid respectively [-]
h	Separation distance [m]
H_f	Mean curvature [m^{-1}]
k	Stiffness [$N \cdot m^{-1}$]
k_c	Capillary bridge stiffness [$N \cdot m^{-1}$]
K	Spreading parameter constant [-]
m	Mass object [kg]
p	Vapor pressure [$N \cdot m^{-2}$]
p_{sat}	Saturated vapor pressure [$N \cdot m^{-2}$]
P	Pressure [$N \cdot m^{-2}$]
P_r	Reflected power [$J \cdot s^{-1}$]
r	Radius [m]
r_1, r_2	Principal radii of curvature [m]
r_K	Kelvin radius [m]
RH	Relative humidity [-]
R	Wetting radius [m]
R_s	Radius of sphere [m]
S	Spreading parameter [$J \cdot m^{-2}$]
t	Time [s]
t_A	Time needed to form one liquid monolayer [s]
t_e	Exposure time [s]
T	Temperature [K]
V	Volume [m^{-3}]
V_m	Molar volume [$m^3 \cdot mol^{-1}$]
W	Work [J]

Greek symbols

α, β	Angle [°]
α_S	Electric polarizability of the solid [$C \cdot m^2 \cdot V^{-1}$]
α_L	Electric polarizability of the liquid [$C \cdot m^2 \cdot V^{-1}$]
γ	Surface energy [$J \cdot m^{-2}$] or surface tension [$N \cdot m^{-1}$]
γ_{SV}	Solid-vapor interfacial energy [$J \cdot m^{-2}$]
γ_{SL}	Solid-liquid interfacial energy [$J \cdot m^{-2}$]
γ_{LV}	Liquid-vapor interfacial energy [$N \cdot m^{-1}$]
θ_A	Advancing contact angle [°]
θ_C	Contact angle [°]
θ_{LV}	Contact angle at the liquid-vapor interface [°]
θ_M	Measured contact angle [°]
θ_R	Receding contact angle [°]
θ_{SL}	Contact angle at the solid-liquid interface [°]
θ_1, θ_2	Contact angle 1 and 2 respectively [°]
κ^{-1}	Capillary length [m]
μ	Friction coefficient [-]
ρ	Density [$kg \cdot m^{-3}$]
ρ_1, ρ_2	Number density interacting objects 1 and 2 [m^{-3}]
ϕ	Roughness ratio [-]

Constants

k_B	Boltzmann constant Value = 1.3806 [$J \cdot K^{-1}$]
g	Gravitational acceleration Value = 9.81 [$m \cdot s^{-2}$]
R	Universal gas constant Value = 8.31446 [$J \cdot K^{-1} \cdot mol^{-1}$]

1 Introduction

Friction and wear behavior between contacting surfaces is of considerable interest to scientists and engineers alike. In ambient conditions, the presence of water can significantly affect the adhesive and friction forces between two contacting surfaces. The reason being the formation of capillary bridges between the surfaces, resulting in capillary forces that can eighter be attractive or repulsive depending on certain conditions. An attractive force resulting from a concave capillary bridge causes an increase in the effective normal load, thus influencing the friction and wear behavior. On the contrary, a convex capillary bridge and the resulting repulsive force can act as a kind of flexible ball bearing, reducing friction and wear. Therefore, the phenomenon of repulsive capillary forces has received a great deal of interest in recent years due to its relevance to the fields of tribology, nanolithography, and microelectromechanical systems (MEMS) [1].

The purpose of this research is to quantify under what conditions repulsive capillary forces occur and how the effect can be produced in practice. Firstly, a mathematical model has been developed which can be used to calculate the capillary force for the case where two planar solids with equal contact angles are considered. Furthermore, a procedure to apply a hydrophobic self-assembled monolayer to a silicon wafer has been established. To study capillary forces, ramping and friction force experiments were conducted. On the microscale, ramping experiments were performed by utilizing an atomic force microscope. On the macroscale, friction force experiments were conducted using a tribometer.

The structure of this thesis is as follows. In Chapter 2, the theoretical framework is presented, addressing topics like surface tension, wettability, and the contact angle. Furthermore, the origin and mechanics of capillary forces are discussed. Additionally, a mathematical model describing repulsive capillary forces is introduced. The experimental setup and methodology are discussed in Chapter 3. In Chapter 4, the results are presented and discussed. The conclusion of this work is discussed in Chapter 5, and in Chapter 6 recommendations for future experiments are provided.

This thesis was written as part of the graduation internship of the Applied Physics program at The Hague University of Applied Sciences, conducted at the Advanced Research Centre for Nanolithography (ARCNL). ARCNL is a public-private partnership between the University of Amsterdam (UVA), The Vu Amsterdam, the Netherlands Organization for Scientific Research (NWO), and ASML [2]. As a member of the Contact Dynamics Group, which focuses on the fundamental aspects of friction and wear of surfaces, the effect of repulsive capillary forces at the macro and microscale has been investigated. Since the potential applications of this research are a trade secret, they are purposefully left out.

2 Theoretical Framework

2.1 Surfaces and Capillarity

Interaction between a material and the exterior environment is mediated by the atoms and molecules at the surface, thus both physical and chemical properties of a material depend on the nature of its surface. Whether examined in bulk or at the nanoscale, atoms and molecules in the interior of a material exhibit different behavior when compared to the same atoms and molecules that exist at the surface. This difference is manifested, for example, in an enhanced reactivity and an altered structure [3].

A surface layer typically consists of three or fewer layers of atoms or molecules [3]. These surface atoms and molecules have fewer nearest neighbors, resulting in an inherent instability in the form of dangling bonds (free radicals). In a dangling bond, the valance of immobilized atoms is unsatisfied, leading to a tendency to chemically and physically interact with the environment [3]. In other words, surface atoms and molecules are in an energetically unfavorable state, lowering their stability. Thus, the energy available for interaction is increased. This extra free energy is therefore called surface energy or *interfacial energy* [3].

2.1.1 Surface Tension

To increase the surface area of a material, atoms or molecules must be relocated from the bulk volume where they are stable into the surface layer where they are inherently less stable. To achieve this, energy must be supplied. For solids, the work required is described in terms of surface energy [$J \cdot m^{-2}$], and for liquids in terms of surface tension [$N \cdot m^{-1}$], although they are qualitatively equivalent. When compared to solids, the intermolecular forces in a liquid are relatively weaker, subsequently allowing the liquid to rapidly respond to deformation such that the liquid reassembles itself to minimize its surface area, a state of minimum energy. In the bulk volume of a liquid, the attractive cohesive forces that hold the liquid together are balanced in all directions. At the surface, however, atoms and molecules have slightly less than half of their nearest neighbors, resulting in a net force that causes the liquid to contract. This phenomenon is called *surface tension* γ, which can be viewed as a stretched elastic membrane that resists deformation.

Suppose a liquid is deformed, such that the surface area A is increased by an amount dA. The work required to increase the area is proportional to the number of atoms or molecules that must be relocated from the bulk volume to the surface. The work required is expressed as [4]

$$dW = \gamma \cdot dA. \tag{1}$$

In other words, the surface tension is the energy required to stretch the surface of the liquid by one unit area. The surface tension of a liquid depends on the intermolecular cohesive interaction of molecules at the surface and environmental factors such as temperature and pressure. Typical values range from ~20 $mN \cdot m^{-1}$ for oils to 72.75 $mN \cdot m^{-1}$ for water at 20 °C [5]. In water, for example, it is the hydrogen bonding between the H_20 molecules that give rise to its characteristic surface tension. In nature, small insects like the water strider can walk on water because their weight is supported by the surface tension of the water.

2.1.2 Contact Angle and Wettability

The surface energy of a solid can be estimated by performing contact angle measurements, whereby a parameter called the *contact angle* θ_C is measured against well-characterized liquids. A given system has a unique contact angle at a certain pressure and temperature, and the contact angle is defined as the angle made by a liquid droplet on a solid surface at the three-phase boundary (also known as the triple line), as is illustrated in Figure 1. The three-phase boundary is the boundary between the solid, liquid, and vapor phase. Aside from the surface tension of the liquid, the contact angle depends on the surface energy of the solid, and its topography and geometry, to name a few [5].

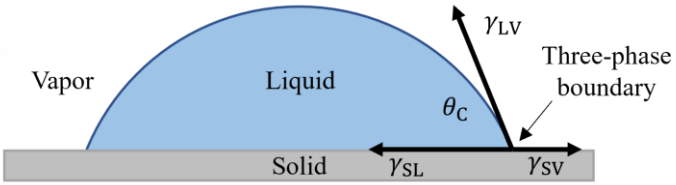

Figure 1: A liquid droplet on the surface of a solid. The contact angle θ_C is measured at the three-phase boundary, the boundary between the solid, liquid, and vapor phase.

Three interfacial energies must be considered: the solid-vapor γ_{SV}, the solid-liquid γ_{SL}, and the liquid-vapor γ_{LV} interfacial energy. Assuming that the system is in thermodynamic equilibrium (that is, there is no net flow of matter or energy in or out of the system), the relationship between the contact angle and the energy at each interface is given by Young's equation [3, 4]. The total interfacial energy of the static system equals to 0, such that

$$\gamma_{SV} - \gamma_{SL} - \gamma_{LV} \cos\theta_C = 0. \tag{2}$$

This can be rewritten as

$$\cos\theta_C = \frac{\gamma_{SV} - \gamma_{SL}}{\gamma_{LV}}. \tag{3}$$

The contact angle is indicative of a phenomenon called *wettability*, as it correlates the surface energy of a solid to the surface tension of a liquid. Wetting is the ability of a liquid to spread on the surface of a solid, and the magnitude of its spread is an indicator of the surface energy of the solid [4]. If a droplet spreads outwards after application, the surface of the solid has enough energy to overcome the surface tension of the water, thereby increasing the interfacial area between the solid and liquid. To put it in another perspective, if the droplet forms up in a bead, the cohesive forces that hold the droplet together are greater than the adhesive forces between the liquid and solid. The surface of a solid exhibits good wetting if the contact angle is between 0 and 90°, and poor wetting if the contact angle is between 90 and 180° [3]. On a more fundamental level, the wettability criterion is not the surface tension of the liquid, but the spreading parameter S, which is given by

$$S = K(\alpha_S - \alpha_L)\alpha_L, \tag{4}$$

where K is a constant, and α_S and α_L are the electric polarizabilities of the solid and liquid respectively [4]. The sign of S, therefore, indicates whether a surface is wettable or not. If $\alpha_S > \alpha_L$, the liquid is less polarizable than the solid, the parameter S is positive and the liquid spreads out completely, as is shown in Figure 2.a. Conversely, if $\alpha_s < \alpha_L$, partial wetting

occurs, causing the liquid to form a spherical cap (Figure 2.b) or a bead (Figure 2.c). For the case where the liquid is water, a surface is designated *hydrophilic* when θ_C < 90°, and superhydrophilic when θ_C < 10°. In contrast, when θ_C > 90° the surface is designated hydrophobic, and superhydrophobic when θ_C > 150° [6].

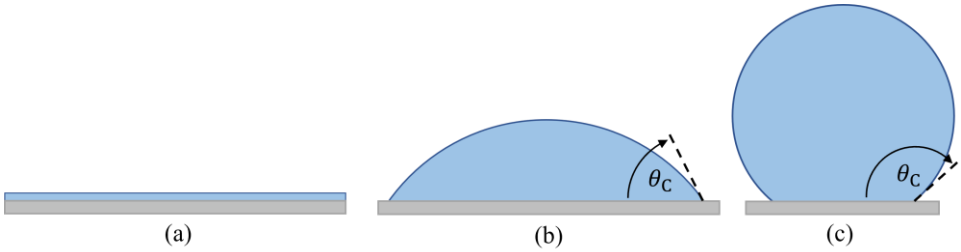

Figure 2: Display of three wetting regimes. (a) A fully wetted surface, (b) a partially wetted hydrophilic surface (θ_C < 90°), and (c) a partially wetted hydrophobic surface (θ_C > 90°).

■ Contact Angle Hysteresis

The contact angle described by Equation (3) assumes a liquid drop on an ideal solid surface; clean, smooth, and chemically homogenous. However this is often not the case, as a surface can be contaminated, has a roughness, and is chemically heterogeneous. On a non-ideal surface, if the volume of the droplet is increased, the contact angle can exceed θ_C without shifting the wetted perimeter. If the volume is increased further, eventually a threshold value θ_A is reached beyond which the wetted perimeter does shift. This threshold value θ_A is called the *advancing contact angle*. Likewise, if the volume of a droplet is decreased, the wetted perimeter does not shift until a certain threshold value θ_R is reached, called the *receding contact angle*. The difference between θ_A and θ_R is the *contact angle hysteresis*. In general, the contact angle θ_C observed during contact angle measurements depends substantially on the way a sample is prepared.

2.1.3 Altering surface wettability

The wettability of surfaces can be altered by coating the surface with organic hydrophobic films. Organic films can be categorized as *self-assembled monolayers* (SAMs) and Langmuir-Blodgett (LB). LB films bond with the surface of a solid by weak van der Waals forces, while SAMs form strong covalent bonds with the surface [7]. For SAMs, the hydrophobic properties make them appealing for use in several applications, such as MEMS and micro-tribology. In addition, micro-patterns can be introduced to a surface to enhance its hydrophobic properties.

■ Self-Assembled Monolayers

A SAM is a molecule that bonds to an activated surface through a process called self-assembly. A distinct characteristic of self-assembly is that the process occurs without requiring excess energy, meaning that the process operates in thermodynamic equilibrium and there is no need for a catalyst. [3]. A SAM consists of a surface-active head group, a body, and a functional group. The head groups bond to the surface by chemical interaction, while the bodies form rigid monolayers due to lateral van der Waals forces between each molecule. The functional groups dictate the properties of the SAM, such as wettability and chemical resistance, to name a few. A commonly used SAM is the molecule octadecyltrichlorosilane (OTS), a silane with chemical formula $CH_3(CH_2)_{17}SiCl_3$. In the context of this work, a brief description is provided regarding the coating of a silicon surface with OTS.

The process of coating an oxidized silicon surface with OTS is called silanization and is illustrated in Figure 3. In the first step of the silanization process, the surface is activated to expose reactive hydroxyl (OH) groups, a process called hydroxylation. Surface activation is usually done by utilizing a Piranha solution (a mixture of water, sulfuric acid (H_2SO_4), and hydrogen peroxide (H_2O_2)), usually in combination with UV-Ozone treatment. In the presence of water, hydrolyzation (not to be mistaken with hydroxylation) is commenced by placing the activated surface in a solution consisting of the OTS and a solvent, hereby functionalizing the surface. Here, the silicon atoms present in the OTS react with the OH groups on the surface to form stable covalent siloxane linkages (Si-O-Si), forming a monolayer in the process. In most applications, monolayers are desired. However, multilayers can be achieved by increasing the concentration of OTS in the solution [6]. The wettability of the modified surface is governed by the extent to which the OTS covers the surface, the remaining unreacted groups from both the OTS and surface, and the density distribution of the OTS [6]. OTS applied to a silicon surface is known to be quite stable at low temperatures but degrades at temperatures above 100 °C in air [7]. Values of the contact angle of water on OTS functionalized surfaces have been reported to range from 100 up to 120°, depending heavily on how the procedure is performed [6, 7, 8].

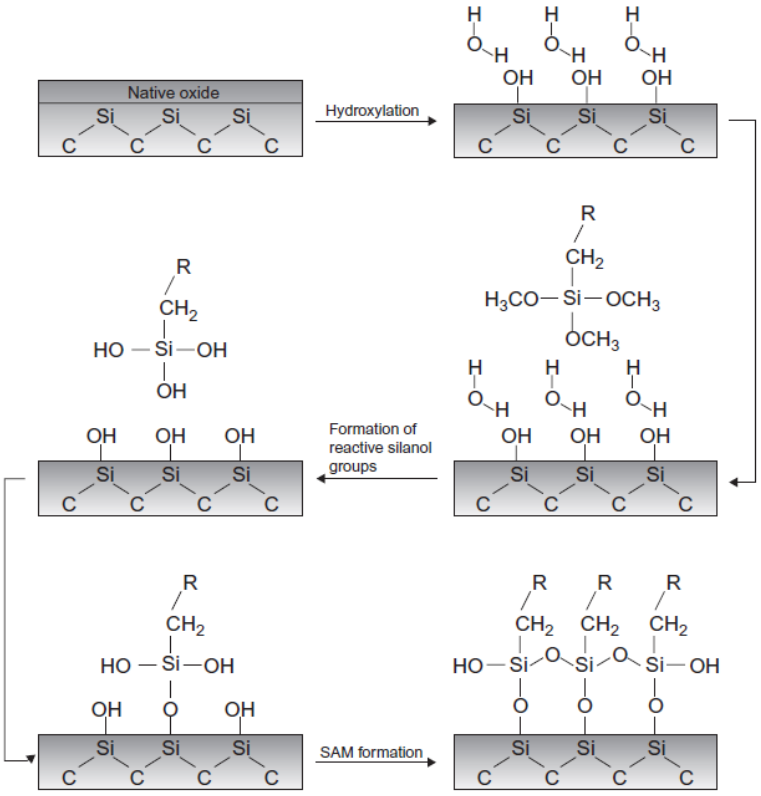

Figure 3: Schematic illustration of the salinization of silicon. Hydroxylation is achieved by Piranha and UV-Ozone treatment, hereby activating the surface. Water can be added, or it may come from the water vapor present in the ambient. Functionalization occurs when the OTS molecules react with the OH groups on the surface, resulting in the formation of a monolayer [9].

■ Micro-patterns

The roughness of the surface of a solid substantially affects the contact angle, enhancing the wettability. If a liquid wets a rough surface homogenously (that is, the grooves are fully wetted), the droplet is in a Wenzel state, as is illustrated in Figure 4.a. When considering water

as the liquid, a hydrophilic surface becomes even more hydrophilic, while a hydrophobic surface becomes more hydrophobic [4]. The measured contact angle θ_M is given by

$$\cos(\theta_M) = \phi \cos(\theta_C), \tag{5}$$

where θ_C is the contact angle on a smooth surface, and ϕ is the roughness ratio of the surface [10]. The roughness ratio is defined as the ratio between the actual surface and the projected surface, where $\phi = 1$ for a smooth surface and $\phi > 1$ for a rough surface [10]. From Equation (5) it is evident that for a surface with a certain roughness, θ_M decreases if the surface is hydrophilic but increases if the surface is hydrophobic. On a rougher surface, however, it becomes more difficult for the water to fully permeate the groves, trapping small air pockets underneath. As a result, the droplet is in a Cassie-Baxter state (Figure 4.b), hereby heterogeneously wetting the surface. In this case, the measured contact angle is described by

$$\cos(\theta_m) = f_1 \cos(\theta_{SL}) + f_2 \cos(\theta_{LV}), \tag{6}$$

where f_1 and f_2 are the fractional surface areas of the solid and the air gaps respectively, and θ_{SL} and θ_{LV} are the contact angles at the solid-liquid and liquid-vapor interface [10]. Note that $f_1 + f_2 = 1$. Air creates a contact angle of 180° with the liquid, hence the second term in the right side of equation (6) reduces to $-f_2$. In any case, the hydrophobicity of the surface is increased. To achieve superhydrophobicity, micro-patterns can be introduced to the surface, hereby exceeding a contact angle of 150° [6]. Here, the fractional area of the solid f_1 should be made as low as possible. In nature, for instance, the superhydrophobic surface of a lotus leaf displays water repulsion and self-cleaning properties due to the structural composition of its leaves and the resulting Cassie-Baxter phenomena.

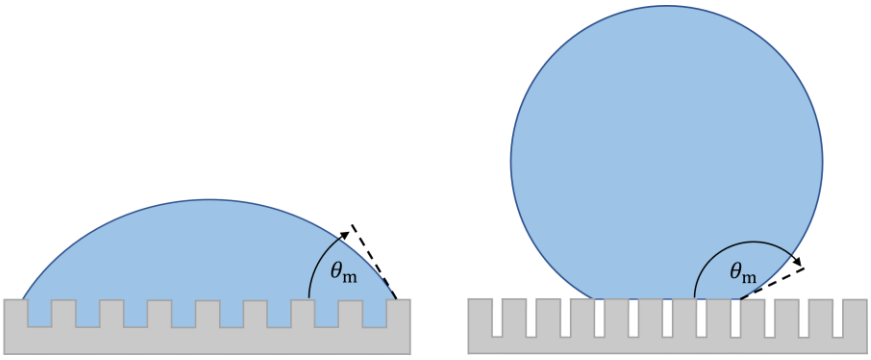

Figure 4: The contact angle θ_m of a droplet on a micro-patterned surface. (a) A water droplet in a Wenzel state and (b) a water droplet in a Cassie-Baxter state. The roughness is illustrated with exaggerated proportions for representation purposes.

2.1.4 Capillary Condensation

In a closed system, the vapor pressure p is defined as the pressure exerted by a vapor in thermodynamic equilibrium with its condensed phase at a given temperature and ambient pressure [4]. When the system is in equilibrium, the rate of evaporation is equal to the rate of condensation. In this state, the saturation vapor pressure p_{sat} is reached. A vapor pressure greater dan the saturation vapor pressure results in the condensation of the vapor into its condensed (liquid) phase. Remarkably, in a porous medium, water vapor can condense below the saturation pressure, allowing the formation of menisci. This phenomenon is called *capillary*

condensation and is a result of increased van der Waals interactions between the molecules in the vapor and the surrounding cavity [11]. The Kelvin equation can be used to relate the curvature of a meniscus to its vapor pressure.

■ The Kelvin Equation

In general, the Kelvin equation [3] describes the vapor pressure exerted by a liquid due to its curved liquid-vapor interface and can be expressed as

$$\ln\left(\frac{p}{p_{\text{sat}}}\right) = \frac{\Delta P V_{\text{m}}}{RT}, \tag{7}$$

where V_{m} is the molar volume of the liquid, ΔP is Laplace pressure, R is the universal gas constant, and T is the temperature. Consider, for example, a liquid confined between the walls of a tube, as is illustrated in Figure 5. The liquid has either an affinity or aversion to adhere to the walls. If the liquid adheres to the wall, the adhesive forces between the liquid and solid are greater than the cohesive forces within the liquid, resulting in the formation of a concave meniscus (Figure 5.a). Conversely, if the cohesive forces within the liquid are stronger than the adhesive forces, a convex meniscus will form (Figure 5.c).

For a concave meniscus, the vapor pressure p exerted by the liquid is less when compared to the vapor pressure of a planar surface (Figure 5.b). In this case, the radius of curvature r is defined from the vapor phase and has, by convention, a negative sign. Contrarily, for a convex meniscus, r is defined from the liquid phase and has a positive sign. The vapor pressure of a convex meniscus is greater since the molecules at the surface have fewer nearest neighbors, resulting in less attractive cohesive forces. Less energy is therefore required for the molecules to escape from the liquid and evaporate. The growth of water droplets in the atmosphere, for instance, can be explained by the Kelvin equation. Small droplets have a relatively high vapor pressure and therefore a relatively high evaporation rate. As a result, they will condense into larger droplets.

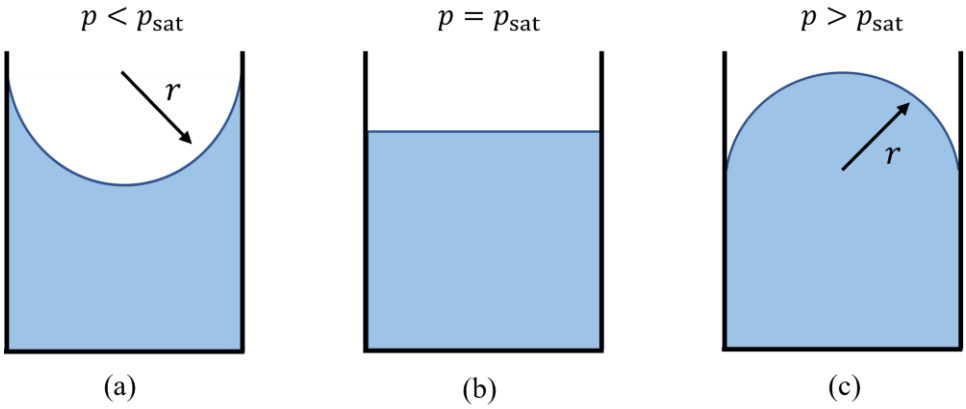

Figure 5: A liquid confined between the walls of a tube. (a) The liquid forms a concave meniscus, (b) the surface of the liquid is planar, and (c) the liquid forms a convex meniscus.

The Kelvin equation can be written such that the vapor pressure can be related to the mean curvature of a meniscus by substituting $\Delta P = 2\gamma/r$ (discussed in more detail in Section 2.1.1):

$$\ln\left(\frac{p}{p_{\text{sat}}}\right) = \frac{2\gamma V_{\text{m}}}{rRT}, \tag{8}$$

where r is the mean curvature of the curved liquid-vapor interface. The percentage ratio between the vapor pressure and the saturation vapor pressure is commonly known as the relative humidity (RH), which is expressed by

$$\mathrm{RH}(\%) = \frac{p}{p_{\mathrm{sat}}} \cdot 100. \tag{9}$$

■ Thickness and Structure of Absorbed Water Films

The extent to which water absorbs on surfaces is governed by relative humidity. Firstly, nucleation must commence for the phase transition from vapor to liquid to occur. From classical nucleation theory it is known that water vapor condenses more readily on hydrophilic surfaces when compared to hydrophobic surfaces. Reason being that, for hydrophilic surfaces, the nucleation energy barrier is reduced, thus increasing the probability of the nucleation process to occur [12]. However, condensation on hydrophobic surfaces is not prohibited.

The thickness and structure of a water layer condensed on a surface can vary significantly depending on the chemical composition of the surface and RH. On hydroxylated hydrophilic silicon, for example, water absorbs into a thin film and the water molecules form an ordered ice-like structure a few layers thick, followed by a disordered structure, as is shown in Figure 6.a. The average thickness of the water film is reported to be in the order of a few nm [13], depending on the RH. On hydrogenated hydrophobic silicon (Figure 6.b), water clusters are formed in a disordered structure with an average thickness of less than 1 nm [13].

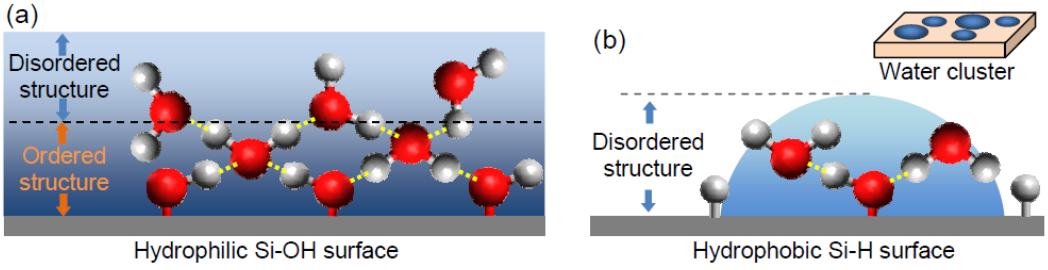

Figure 6: Schematic illustration of the structure of an absorbed water layer on (a) a hydroxylated silicon surface and (b) a hydrogenated silicon surface. The yellow dotted lines are the hydrogen bonds between the H_2O molecules. [13]

2.1.5 Capillary Bridge

In the field of surface science, a water meniscus formed between two solids is also known as a *capillary bridge*. An example of capillary bridges formed between asperities of two surfaces in the presence of absorbed water layers is shown in Figure 7. As is illustrated, capillary bridges form between both contacting and near contacting asperities. For a volume V of undersatured vapor to start condensing into a capillary bridge, a threshold energy barrier ΔE cost must be surpassed. This threshold energy barrier is given by

$$\Delta E \approx k_{\mathrm{B}} T \ln\left(\frac{p_{\mathrm{sat}}}{p}\right) \rho \mathrm{V}, \tag{10}$$

where k_{B} is the Boltzmann constant, T is the temperature and ρ is the density of the water [11]. The threshold energy barrier depends on surface roughness, the number of asperities, and

chemical heterogeneities. Based on the law of Arrhenius, the time needed to condense a capillary bridge of height h can be estimated by

$$t = t_A e^{\frac{\Delta E}{k_B T}}, \tag{11}$$

where t_A is the time needed to form one liquid monolayer [11]. Riedo et al. have experimentally demonstrated that the time it takes to condense one monolayer to be 25 μs [14]. Furthermore, it is known that from the literature that a capillary bridge in thermodynamic equilibrium becomes unstable and breaks once a critical distance $D_C \approx (4\pi V)^{1/3}$ is attained [10].

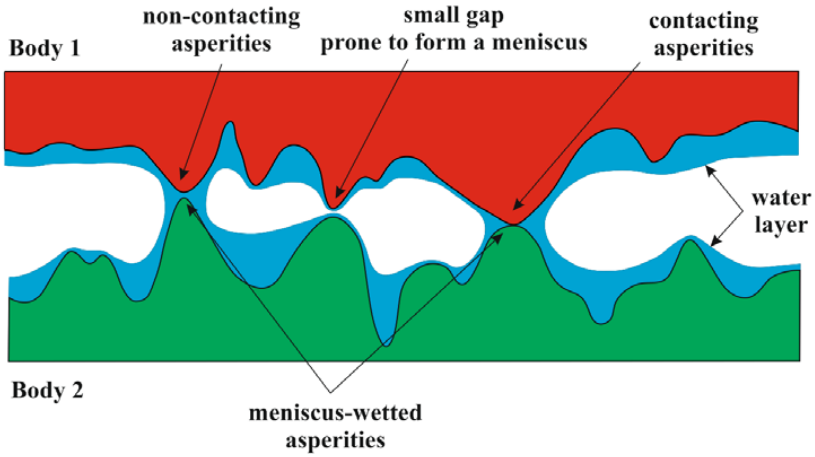

Figure 7: Schematic illustration of capillary bridges formed between two contacting surfaces in the presence of absorbed water layers. The capillary bridges form between contacting and near-contacting asperities. [15]

2.2 Capillary Forces

An attractive capillary force between two contacting surfaces increases the normal load and hence, negatively affecting their friction and wear behavior. On the contrary, capillary bridges that exert a repulsive force reduce friction. To quantitively and qualitatively study the forces acting between contacting or near-contacting surfaces due to the formation of capillary bridges, a characterization technique called Atomic Force Microscopy (AFM) is often employed. The force between an AFM probe and a substrate is described by *the adhesive force*. The total adhesion force F_{adh} consists of the following:

$$F_{adh} = -F_{cap} + F_{vdW} + F_{el} + F_B. \tag{12}$$

where F_{cap} is the capillary force due to the capillary bridge, F_{vdW} is the force due to intermolecular van der Waals interactions between the probe and the substrate, F_{el} is the electrostatic force due to a charge difference between probe and substrate, and F_B is the chemical bonding force due to physisorption and chemisorption of molecules of one surface on another when in hard contact [16]. In Equation (12), notice the negative sign of the capillary force. If the capillary is repulsive (F_{cap} is positive), the adhesion force is decreased. The opposite is true when the capillary is attractive.

During experiments, the probe and substrate are usually exposed to the ambient for a prolonged time. Thus, no net charges are expected to remain, such that F_{el} = 0. The surfaces are assumed to be saturated with chemical bonds, hence the chemical bonding force F_B = 0. Therefore, the

capillary force and the van der Waals forces are the main contributors to the adhesion force. For a sphere-plane geometry, the van der Waals force between the two objects is given by

$$F_{\mathrm{vdW}} = \frac{A_{\mathrm{H}} R_{\mathrm{s}}}{6a^2}, \tag{13}$$

where A_{H} is the Hamaker constant, R_{s} is the radius of the sphere, and a is the distance between the two objects [16]. The Hamaker depends on the dielectric properties of the interacting objects and the medium between them:

$$A = \pi^2 C \rho_1 \rho_2 , \tag{13}$$

where C is the London coefficient is the particle-particle pair interaction of the medium, and ρ_1 and ρ_2 are the number densities of the two interacting objects [10]. Values for the Hamaker constant range in order of 10^{-19} to10^{-20} J depending on the medium [3]. For a given system of interacting objects, the Hamaker constant, hence the van der Waals force, is greater if the objects are in air than in water.

■ Adhesive Force Dependency on the Relative Humidity

The influence of RH on the adhesive force has been investigated to a large extend by various authors. The published results are ambiguous, however, as some papers report an increase of the adhesion force on hydrophilic substrates with an increase in RH, while others observed a decrease or even no RH dependency [16, 17]. A review by H. Nasrallah concludes that the adhesive force of a hydrophilic probe on hydrophilic substrates shows an RH dependence, while hydrophobic substrates show hardly any dependency [18]. Concerning hydrophilic substrates, the RH dependency is supported by the formation of capillary bridges, resulting in an attractive capillary force, increasing the adhesive force. Conversely, the lack of capillary bridge formation due to weak capillary condensation on hydrophobic substrates results in no RH Dependence, as is illustrated in Figure 8.

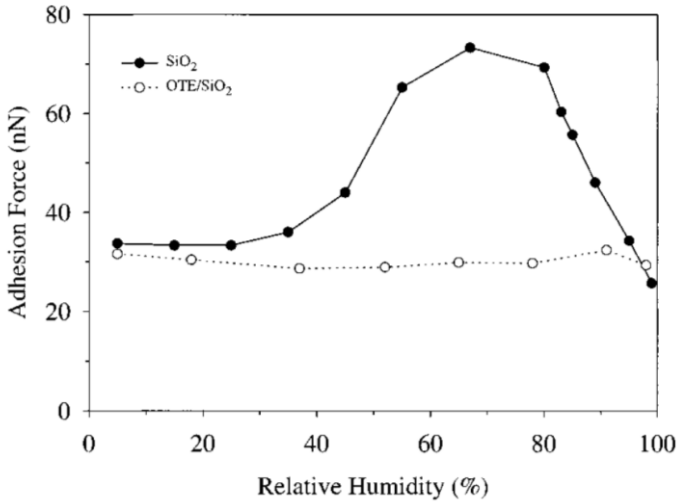

Figure 8: The adhesion force as a function of the relative humidity. The adhesion force is measured with a hydrophilic Si_3N_4 tip against a hydrophilic SiO_2 substrate and a hydrophobic OTE/SiO_2 substrate. [16]

2.2.1 The Laplace Pressure

The Young-Laplace equation relates the pressure difference between the inside and outside of a curved liquid interface to its mean curvature and is fundamental to the study of capillary forces. This pressure difference is called the *Laplace pressure* ΔP, and originates from the surface tension γ_{LV}, hereafter denoted as γ, at the liquid-vapor interface [4].

Consider a concave and convex capillary bridge between two planar surfaces, as is illustrated in Figure 9. The sign convention is such that r_1 is always positive and r_2 is eighter negative or positive whether the liquid-vapor interface is concave or convex respectively. The Laplace pressure is given by

$$\Delta P = P_{\text{in}} - P_{\text{out}} = 2H_{\text{f}}\gamma = \gamma\left(\frac{1}{r_1} + \frac{1}{r_2}\right), \tag{14}$$

where P_{in} and P_{out} are the pressure inside and outside of the curved liquid-vapor interface respectively, H_{f} is its mean curvature, and r_1 and r_2 are the principal radii of curvature [19]. An interface with positive curvature is convex and the pressure difference is positive. On the contrary, if the curvature is negative, the interface is concave and the pressure difference is negative. Moreover, if the capillary bridge is in thermodynamic equilibrium and gravitational effects are negligible, the pressure difference is constant across the capillary bridge and its mean curvature H_f is constant throughout the liquid-vapor interface [19]. Furthermore, if both radii are equal ($r_1 = r_2$), such as for a sphere, the Laplace pressure simplifies to

$$\Delta P = \frac{2\gamma}{r}. \tag{15}$$

For instance, a water droplet (γ = 72.75·10^{-3} N·m^{-1}) with a radius of 5 mm has a Laplace pressure of ~30 N·m^{-2}, while a microscopic droplet with a radius of 5 µm has a Laplace pressure of ~30·10^{3} N·m^{-2}, which is a substantial amount.

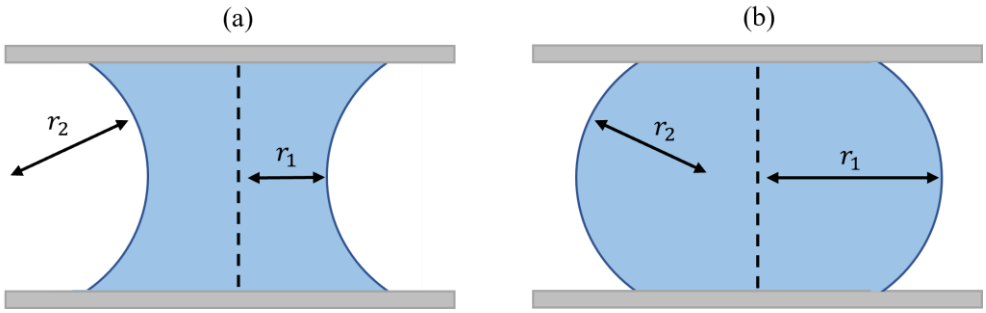

Figure 9: The principal radii r_1 and r_2 of (a) a concave capillary bridge and (b) a convex capillary bridge. For a concave bridge r_1 is positive and r_2 is negative. For a convex bridge r_1 and r_2 are positive.

■ The Kelvin Radius

As mentioned prior, capillary condensation allows for the formation of capillary bridges between near-contacting surfaces. The distance at which the liquid phase is favorable over the vapor phase is governed by the *Kelvin radius* r_{k} [10], which is given by

$$r_{\text{k}} = \left(\frac{1}{r_1} + \frac{1}{r_2}\right)^{-1}. \tag{16}$$

The Kelvin radius is an important quantity in AFM. If the curvature of the probe or distance between the probe and substrate is smaller than $|r_k|$, the probe will act as a nucleation center for the condensation of a capillary bridge [4]. In ambient conditions and at room temperature (20 °C), the kelvin radius for water is [10]

$$r_k[\text{nm}] = \frac{0.54}{\ln\left(\frac{p}{p_s}\right)} = \frac{0.54}{\ln\left(\frac{\text{RH}}{100}\right)}. \tag{17}$$

For instance, $r_k \approx$ -5.1 nm at RH = 90%, $r_k \approx$ -0.78 nm at RH = 50%, and $r_k \approx$ -0.23 nm at RH = 10%. As a consequence, capillary bridges that form due to capillary condensation have nanometer-scale sizes.

■ The Capillary length

The capillary length, denoted as κ^{-1}, is characterized as the length beyond which gravity influences the shape of a capillary bridge (or menisci more generally speaking) [4]. It is a fundamental physical property that relates the gravity force to the forces due to the surface tension of a liquid. By comparing the Laplace pressure ΔP in a droplet with radius κ^{-1} to the hydrostatic pressure exerted by a liquid with density ρ at depth $2\kappa^{-1}$, the capillary length can be derived. From Equation (14) it is known that the Laplace pressure of a curved liquid-vapor interface is

$$\Delta P = P_l = \frac{2\gamma}{r} = \frac{2\gamma}{\kappa^{-1}}. \tag{18}$$

The hydrostatic pressure exerted by a liquid due to gravity is given by

$$P_h = \rho g h = 2\rho g \kappa^{-1}. \tag{19}$$

Thus, the length at which Laplace pressure is equal to the hydrostatic pressure, $P_l = P_h$, is

$$\kappa^{-1} = \sqrt{\frac{\gamma}{\rho g}}. \tag{20}$$

For water on earth at room temperature, the gravitational acceleration g = 9.81 m·s^{-2}, the surface tension of water γ = 72.75 · 10^{-3} N·m^{-1} and the density of water ρ = 997 kg·m^{-3}, thus $\kappa^{-1} \approx$ 2.7 mm. For menisci with a size κ^{-1} < 2.7 mm, the capillary forces dominate, and the effect of gravity its shape is negligible, resulting in constant mean curvature H_f.

2.2.2 The Capillary Force

The formation of a capillary bridge between two surfaces results in a *capillary force*. The magnitude and direction of the capillary force depend mainly on the wettability and geometry of both surfaces, the wetted area at contact with the surfaces, and the surface tension of water. If the capillary bridge is stretched or compressed, the separation time and viscosity of the liquid also affect the capillary force. However, the effect of viscosity is only significant when the separation time is short, and the capillary bridge is relatively large [18]. The geometry or profile of the capillary bridge dictates whether the capillary force is attractive or repulsive.

The subject of capillary forces has been extensively studied throughout the years by various authors, both theoretically and experimentally. There are generally two methods used to model

capillary forces; one that involves the Free-energy approach, and one that involves the Young-Laplace equations. On the theoretical side, different models have been developed considering planar/planar, sphere/planar, and sphere/sphere geometries [20, 21, 18, 22, 19]. On the experimental side, the influence of wettability, humidity, and surface roughness on the capillary force has been investigated thoroughly [17, 23, 22, 19]. The models, however, require a great deal of mathematical insight and a deep understanding of the subject. Thus, for this work, a relatively simple model using the Laplace approach is presented, restricted to the case of two planar surfaces.

■ Tension Force and Laplace Force

Consider Figure 10, illustrating two capillary bridges with equal contact angles between planar solid surfaces, separated by an arbitrary distance. In Figure 10.a, both surfaces are hydrophilic, leading to a concave profile with contact angles θ_1 and θ_2 less than 90°. In Figure 10.b, both the surfaces are hydrophobic, resulting in a convex profile with contact angles θ_1 and θ_2 greater than 90°. The total capillary force F_{cap} acting on both the top and bottom surface is given by

$$F_{\text{cap}} = F_{\text{ten}} + F_{\text{Lap}}, \tag{21}$$

where F_{ten} is the tension force due to the surface tension of the liquid, and F_{Lap} is the Laplace force due to the Laplace pressure. For the system to be in equilibrium (that is, stationary), it is important to note that the forces acting on the top surface must be equal but opposite to the forces acting on the bottom. If F_{cap} is positive, the capillary bridge exerts a repulsive force on both surfaces. On the contrary, if the capillary bridge exerts an attractive force on both surfaces, F_{cap} is negative.

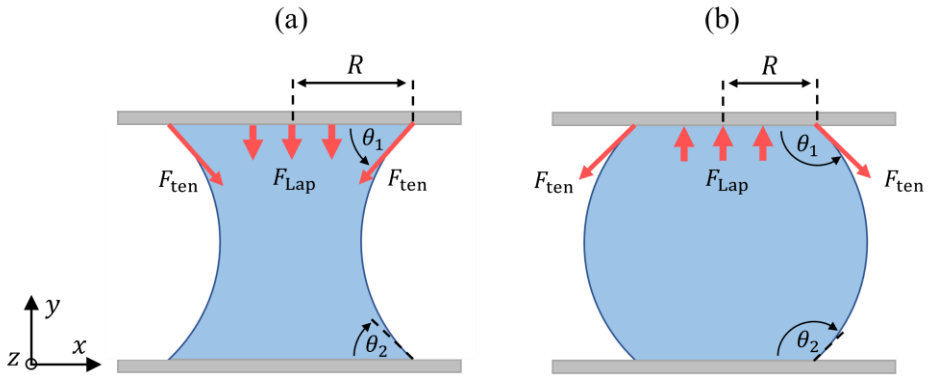

Figure 10: Display of the tension force and Laplace force acting on the top solid surface for (a) a concave capillary bridge and (b) a convex capillary bridge. By convention, the forces acting downwards in the y-direction are regarded as negative, whereas forces acting upwards are positive. The magnitude of the forces is not to scale for illustration purposes.

If the forces acting at the top surface in Figure 10 are examined, the tension force acts along the wetted perimeter ($2\pi R$) with a vector that is tangential to the liquid-vapor interface at the three-phase boundary (that is, alongside θ_1). Radius R is therefore conveniently called the wetting radius. The x-components of the tension force are balanced; thus the resultant tension force acts solely along the y-direction. Thus, the tension force is given by [5]

$$F_{\text{ten}} = 2\pi R\gamma \sin\theta_1. \tag{22}$$

The Laplace force acts in the normal direction to the surface of the wetted area (πR^2), likewise acting along the y-direction. The Laplace force is given by [5]

$$F_{\text{Lap}} = \pi R^2 \Delta P = \pi R^2 \gamma \left(\frac{1}{r_1} + \frac{1}{r_2}\right). \tag{23}$$

Note that r_2 is negative for a concave profile. As is evident from Equation (23), to calculate the Laplace force, information about the principal radii of curvature r_1 and r_2 is required. A more elaborate description of the profile of the capillary bridge is therefore necessary. When examining Figure 10, it becomes apparent that the tension force is, at least in the case of two planar surfaces, negative for either case. The Laplace force can eighter be negative or positive depending on whether the profile is concave or convex respectively. The Laplace force of a concave capillary bridge can be positive, however, under the condition that $1/r_1 > 1/r_2$.

2.2.3 Repulsive Capillary Force Model

The emphasis of this work is on repulsive capillary forces, thus a more detailed description is provided for a convex capillary bridge, as is shown in Figure 11. The parameters that influence the profile are contact angles θ_1 and θ_2, the separation distance h between the top and bottom surface, and the volume V of the capillary bridge. However, a few assumptions must be made to appropriately define the model. The capillary bridge is assumed to be in thermodynamic equilibrium, so evaporation of the capillary bridge due to the Laplace pressure does not occur. Furthermore, the size of the capillary bridge is smaller than the capillary length κ^{-1}, such that the influence of gravity on the profile is considered to be negligible. Moreover, both surfaces are considered to be smooth and chemically heterogeneous, thus contact angle hysteresis is of no effect. Therefore, contact angles θ_1 and θ_2 are assumed to be equal ($\theta_1 = \theta_2 = \theta_C$), which will simplify the calculations considerably. It is once again important to note that, in these conditions, the Laplace pressure is constant across the entire interface of the capillary bridge, and the mean curvature H_f is constant throughout the liquid-vapor interface. With the aforementioned assumptions in mind, a mathematical model is presented that can be used to calculate the tension force, Laplace force, and the total capillary force.

The principal radii of curvature (see Figure 11) are determined by inserting a line normal to the liquid-vapor interface at point P (the bulge), which is the x-axis in this case. Radius r_2 is defined as the curvature of the capillary bridge in the xy-plane. Radius r_1 is the curvature in the xz-plane (perpendicular to the plane of the figure); the distance between the bulge and the y-axis[1]. As mentioned before, R is the radius of the wetted perimeter (or wetted area), and h is the separation distance between the two surfaces. The capillary bridge is axisymmetric and can therefore be divided into four quadrants. The profile in each quadrant is a portion of a circle with radius r_2. As will be clarified, radius r_2 depends on contact angle θ_C and separation distance h, and r_1 depends on volume V and r_2. By thorough examination of any quadrant, r_1 and r_2 can be expressed in terms of θ_C, h and V.

[1] For capillary bridges with asymmetric contact angles, defining r_1 becomes more complicated. For this work, however, the description provided will suffice.

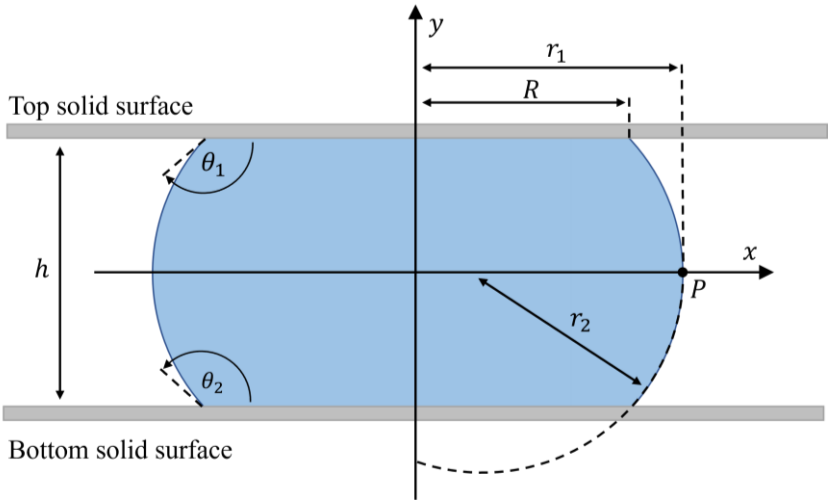

Figure 11: An illustration of a convex capillary bridge between two planar surfaces between two surfaces, separated by a distance h. The contact angles θ_1 and θ_2 are equal. The radius of the wetted area is R, and r_1 and r_2 are the principal radii of curvature. Point P is the buldge.

Figure 12.a. shows a closer examination of the upper-right quadrant of the capillary bridge, where the contact angle is denoted as θ_C, and the distance between the surface of the top solid and the bulge is $h/2$, Two right-angled triangles are drawn with their apex converging at point N; the three-phase boundary. The hypotenuse of the right triangle (Figure 12.b) is tangential to the curvature of the capillary bridge at point N. The hypothenuse of the left triangle is radius r_2, and is perpendicular to the curvature at point N. By applying trigonometry principles and noticing that $\alpha + \beta = 90°$, angle α can be expressed as

$$\alpha = 90 - \beta = 90 - (\theta_C - 90) = 180 - \theta_C. \tag{24}$$

Thus, radius r_2 is given by

$$r_2 = \frac{h}{2\cos\alpha}. \tag{25}$$

Note that $\cos(\alpha) = \cos(180 - \theta_C) = -\cos\theta_C$, therefore Equation (25) can be written as

$$r_2 = \frac{h}{-2\cos\theta_C}. \tag{26}$$

Now that an expression of r_2 is found, radius r_1 can be determined by examining Figure 12.c Since r_2 covers the entire base of the left triangle but only a portion of the right, radius r_1 can be obtained by simply adding that portion of r_2 to R:

$$r_1 = R + r_2 - r_2\sin\alpha = R + r_2(1 - \sin\alpha), \tag{27}$$

where $\sin(\alpha) = \sin(\theta_C)$. By substituting Equation (26) in Equation (27), r_1 is expressed as

$$r_1 = R + \frac{h(1 - \sin\theta_C)}{-2\cos\theta_C}. \tag{28}$$

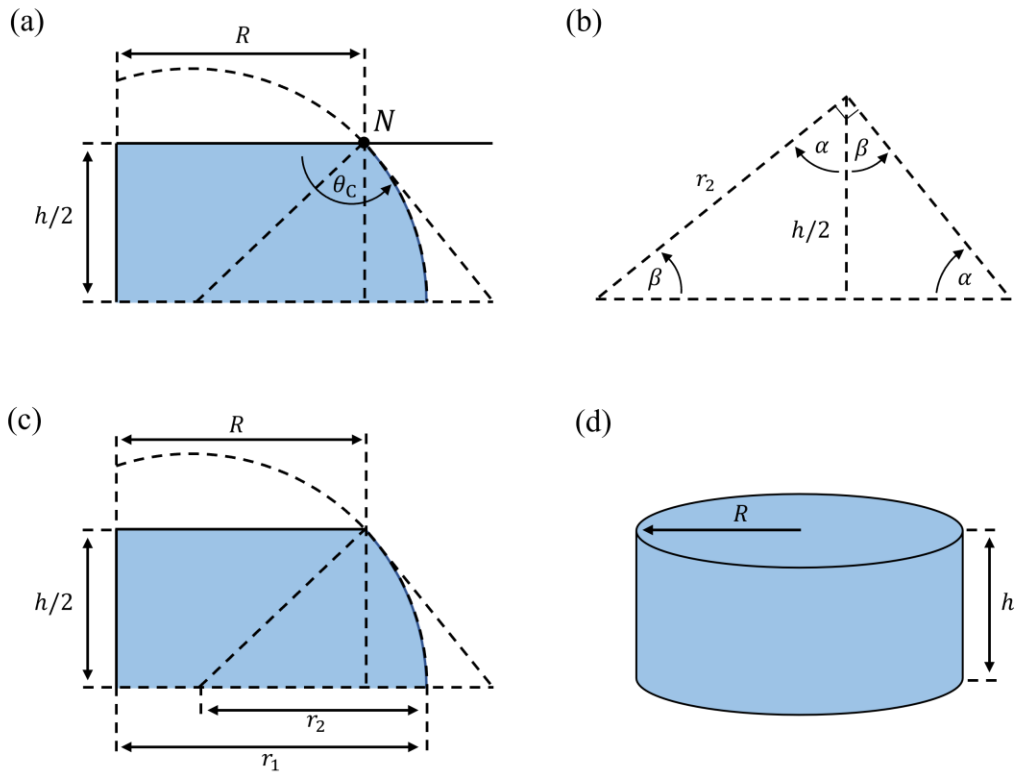

Figure 12: (a) Examination of the upper right quadrant of the capillary bridge. The distance between the top surface and the bulge is $h/2$. (b) A closer inspection of the two right-sided triangles with angles α and β. Radius r_2 is determined by applying trigonometry. (c) The upper right quadrant, now with the determined radii r_1 and r_2 drawn. (d) A cylinder with radius R and height h to approximate the volume of the capillary bridge.

Both r_1 and r_2 are now determined. As is clear by Equation (26), r_2 depends on the separation distance h between the two surfaces. At any given contact angle, by decreasing the separation distance, r_2 will decrease as well, and vise versa. Radius r_1 depends on the wetting radius R, which is indicative of the volume of the capillary bridge (Figure 12.d). Under the condition that $R \gg h$, the volume of the capillary bridge can be approximated by a cylinder, that is

$$V \approx \pi R^2 h, \tag{29}$$

such that

$$R \approx \sqrt{\frac{V}{\pi h}}. \tag{30}$$

By substituting Equation (30) in Equation (28), r_2 is expressed as

$$r_1 = \sqrt{\frac{V}{\pi h}} + \frac{h(1-\sin\theta_C)}{-2\cos\theta_C}. \tag{31}$$

Thus, the tension force (notice the negative sign) is given by

$$F_{\text{ten}} = -2\pi R\gamma \sin\theta_1 = -\sqrt{\frac{4\pi V}{h}}\gamma \sin\theta_C \,, \tag{32}$$

and the Laplace force can be expressed as

$$F_{\text{Lap}} = \pi R^2 \gamma \left(\frac{1}{r_1} + \frac{1}{r_2}\right) = \frac{V\gamma}{h}\left[\frac{1}{\left(\sqrt{\frac{V}{\pi h}} + \frac{h(1-\sin\theta_C)}{-2\cos\theta_C}\right)} + \frac{1}{\left(\frac{h}{-2\cos\theta_C}\right)}\right]. \tag{33}$$

Thus, the total capillary force is given by

$$F_{\text{cap}} = \frac{V\gamma}{h}\left[\frac{1}{\left(\sqrt{\frac{V}{\pi h}} + \frac{h(1-\sin\theta_C)}{-2\cos\theta_C}\right)} + \frac{1}{\left(\frac{h}{-2\cos\theta_C}\right)}\right] - \sqrt{\frac{4\pi V}{h}}\gamma \sin\theta_C \,. \tag{34}$$

Consequently, the total capillary force is repulsive if the Laplace force is greater than the absolute value of the tension force. Equation (34) is valid only if the contacts angles of the surface of both solids are equal, and where the wetting radius is considerably larger than the separation distance ($R \gg h$). When dealing with concave capillary bridges in the same conditions mentioned above, Equation 34 can also be utilized. In that case, the second term between the brackets of the Laplace force (equivalent to $1/r_2$) is negative.

■ Capillary Bridge Profile

So far, only cases have been considered where both contact angles are equal. When the wettability of one surface differs from the other, however, the capillary bridge displays a different profile. Figure 13 demonstrates two cases where the contact angles θ_1 and θ_2 differ from each other. Figure 13.a shows the case where $\theta_1 < 90°$ and $\theta_2 > 90°$ (that is, a hydrophilic and hydrophobic surface respectively). Figure 13.b shows the case where it is the other way around. The curvature is concave for both cases, meaning that r_2 is negative. Without going into too much detail, to calculate the tension and Laplace force, an analytical solution provided by Delaunay can be applied [19]. Recall from Equation (14) that the Laplace pressure is given by $\Delta P = 2H_f\gamma$. The mean curvature H_f can be expressed as [19]

$$H_f = \frac{\sin\theta_1 R_1 - \sin\theta_2 R_2}{R_1^2 - R_2^2}, \tag{35}$$

such that

$$\Delta P = 2\gamma \frac{\sin\theta_1 R_1 - \sin\theta_2 R_2}{R_1^2 - R_2^2}. \tag{36}$$

Equation (36) requires information about the wetted area's R_1 and R_2. On a macroscale, the profile and, thus, wetted areas can be determined optically. On a microscale, a more extensive model provided by Y. Wong et al. [19] can be used. However, this is beyond the scope of this work.

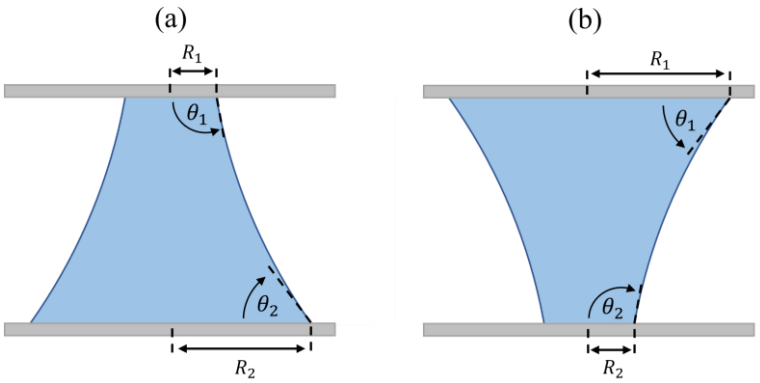

Figure 13: Capillary bridge profile for dissimilar contact angles θ_1 and θ_2. The wetted radius at the top surface is R_1 and the wetted radius at the bottom is R_2.

■ Colloidal probe

During the ramping experiments with the AFM, a colloidal probe is used (see section 3.3). The capillary forces between a sphere/planar geometry are different from what is previously described. Consider the case where a convex capillary bridge is present between a colloidal probe and the planar surface of a solid, as is illustrated in Figure 14. The tension force and Laplace force exerted on the colloidal probe can be expressed in terms of the half-filling angle α. The half-filling angle is the angle made between the center of the colloidal probe with radius R_p and the wetted perimeter (or area). The tension force is given by

$$F_\mathrm{ten} = 2\pi R \sin\alpha \sin(\alpha + \theta_1), \tag{37}$$

and the Laplace force is

$$F_\mathrm{Lap} = \pi R^2 \sin^2\alpha\, \gamma \left(\frac{1}{r_1} + \frac{1}{r_2}\right). \tag{38}$$

Thus, the total capillary force is described by

$$F_\mathrm{cap} = \pi R^2 \sin^2\alpha\, \gamma \left(\frac{1}{r_1} + \frac{1}{r_2}\right) - 2\pi R \sin\alpha \sin(\alpha + \theta_1). \tag{39}$$

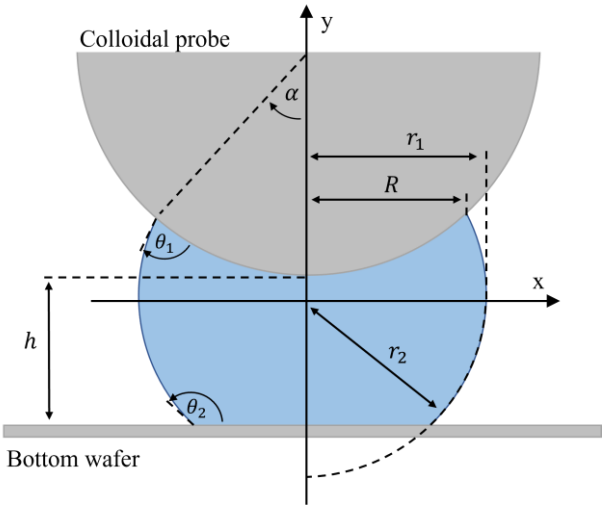

Figure 14: An illustration of a convex capillary bridge between a colloidal probe and a planar surface, separated by a distance h. The contact angles θ_1 and θ_2 are equal. The radius of the wetted area is R, and r_1 and r_2 are the principal radii of curvature. The half-filling angle is α.

2.2.4 Stiffness

A convex capillary bridge exerts a force in the normal direction to the surface of a solid. Depending on the strength of the force and both physical and structural properties of the solid, it is subject to deformation. To what extend a solid deforms is characterized by its stiffness [N·m^{-1}]. In general, the stiffness k of an object is defined as the force required to achieve a certain deformation and can be described by

$$k = \frac{F}{\delta}, \tag{40}$$

where F is the force exerted on the object and δ is the deformation or displacement by the object [24]. As mentioned before, for a given volume of water and contact angle θ_C, the capillary force exerted in the normal direction to a planar surface depends on the separation distance h. Hence, the stiffness of the capillary bridge k_c is determined by differentiating the total capillary force [N] as a function of the separation distance [m], like so

$$k_c = \frac{dF_{cap}}{dh} = \frac{d\left(\frac{V\gamma}{h}\left[\frac{1}{\left(\sqrt{\frac{V}{\pi h}} + \frac{h(1-\sin\theta_C)}{-2\cos\theta_C}\right)} + \frac{1}{\left(\frac{h}{-2\cos\theta_C}\right)}\right] - \sqrt{\frac{4\pi V}{h}}\gamma\sin\theta_C\right)}{dh}. \tag{41}$$

An analytical solution to Equation (38) proved too time-consuming and difficult to solve, thus instead, a numerical approach is opted. For a function $y = f(x)$, the change in y is

$$\Delta y = f(x + \Delta x) - f(x). \tag{42}$$

where x is the argument of the function, and Δy and Δx are the change in y and x respectively. When this principle is applied to Equation (38), the change in the total capillary force because of the change in separation distance is given by

$$\Delta F_{cap} = F_{cap}(h + \Delta h) - F_{cap}(h), \tag{43}$$

where h is the separation distance, and Δh is the change in distance. Thus, the stiffness of the capillary bridge can be described by

$$k_c = \frac{\Delta F_{cap}}{\Delta h} = \frac{F_{cap}(h + \Delta h) - F_{cap}(h)}{\Delta h}. \tag{44}$$

2.2.5 The Influence of Capillary Forces on The Friction Force

On the nanometer scale, the presence of capillary bridges between two contacting or near-contacting surfaces can increase the normal load, thereby affecting adhesion and friction forces. It has been suggested by Riedo et al. that the velocity-dependent forces in sliding friction are due to a superposition of two competitive phenomena [14]. The first is the temperature-depended stick and slip motion, giving rise to a logarithmic increase of friction with increasing velocity. The second is due to the formation of capillary bridges between the contact area of the contacting surfaces, leading to a logarithmic decrease of friction with increasing velocity. Depending on the relative humidity, and the wettability and the roughness of both surfaces, the influence of capillary forces on the friction can have two origins. There can be a change in

friction coefficient, or the adhesion force is affected. The relationship between friction and normal forces for contacting surfaces is [14]

$$F_{\mathrm{F}} = \mu(F_{\mathrm{N}} + F_{\mathrm{adh}}), \tag{45}$$

where μ is the friction coefficient, F_{F} is the friction force, F_{N} is the normal load, and F_{adh} is the adhesion force. The normal force is determined by

$$F_{\mathrm{N}} = m \cdot g, \tag{45}$$

where m is the mass of the top sliding surface and g is the gravitational acceleration. Moreover, the adhesion force, as was established in Equation (12), consists of

$$F_{\mathrm{adh}} = F_{\mathrm{vdW}} - F_{\mathrm{cap}}. \tag{47}$$

The capillary force is humidity dependent, whereas the van der Waals force is not. Hence, no menisci are formed at relatively low RH, and the adhesion force is solely due to the van der Waals interactions between the two contacting surfaces. By inspecting Equations (45 – 47), it is clear that the wettability of both sliding surfaces determines whether the friction force is increased or decreased in the presence of water. If both surfaces are hydrophobic, the capillary bridges present exert a repulsive force, leading to a decrease in the adhesion force and, hence, a decrease in the friction force. In this case, the water is said to be *lubricating* the surface. The opposite is true when both surfaces are hydrophilic.

3 Methodology

3.1 Contact Angle Measurements

3.1.1 OTS Coating Procedure

Most studies done on the subject of hydrophobic organic films with OTS utilize the molecule octadecyltrichlorosilane ($CH_3(CH_2)_{17}SiCl_3$). Due to a delivery problem at the supplier, however, this chemical was not obtainable in time. Thus, the closely related octyltrichlorosilane (97%, Aldrich) with chemical formula $CH_3(CH_2)_7SiCl_3$ was used. This molecule has the same terminal group (CH_3) and surface-active head group ($SiCl_3$), so a similar wettability was expected. Both chemicals can be labeled as OTS. Thus, to differentiate the octyltrichlorosilane used in this work, it is hereafter labeled as OTS'.

Silicon wafers (ID: 452, University Wafer) were used to apply the OTS' coating. The wafers were thoroughly rinsed with ethanol (99.8%, Aldrich) and ultra-pure water, followed by nitrogen blowing. This procedure was repeated three times, after which the wafers were placed in a UV-Ozone cleaner (Type G, Ossila) for 30 mins. The UV-Ozone treatment removes any organic contaminants still present on the surface, while also catalyzing the growth of an oxygen layer on the surface. Following the UV-Ozone treatment, the wafers were left in the ambient air for 5 mins to activate the surface by letting the oxide layer react with the water vapor in the humid air. Thereafter, the wafers were immersed into a 3 mM solution of OTS' (95%, Aldrich) in Toluene (99.6%, Aldrich) for at least 17 hours, the minimum time required for proper OTS' coverage [7].

The colloidal probes (NanoAndMore GMBH) were made from silicon dioxide (SiO_2), and had a diameter of 6.62 μm. For the colloidal probes, a more cautious approach was taken. Since the probes are very fragile and small, the rinsing and drying steps were skipped. The probes were treated directly with the UV-Ozone cleaner and left in humid air for 5 mins. Afterward, the probes were placed in a casing (see Figure 34, Appendix II), with the interior of the casing covered with aluminum foil to prevent the reaction of OTS' with the plastic walling of the casing.

3.1.2 Execution

The contact angle measurements were conducted using the Drop Shape Analyzer 100 (Krüs). Three different samples were prepared and analyzed, namely: a stock wafer, a UV-Ozone treated wafer, and an OTS' coated wafer. Each contact angle measurement was executed as follows. In the DSA software, the setting "sessile drop" was set. Hereafter, the sample orientation was adjusted, followed by the positioning of the needle. After the positioning sample and needle, the optical settings were adjusted such that the needle was into focus, after which a drop was deposited on the sample. Finally, the contact angle was measured by the software. Subsequently, the water droplet was removed, and the stage was cleaned. For each of the three samples, the measurement was repeated 5 times to gather statistics.

3.2 Repulsive Capillary Force Model

A Python script (see Appendix IV) has been written that incorporates the mathematical model presented in Chapter 2. The script can be used to calculate the tension force, the Laplace force, the total capillary force, and the stiffness given the parameters θ_C, V and h, given by Equations (32-34). The separation distance can be set to range from a minimum $h_{\min}$ to a maximum $h_{\max}$.

However, caution must be taken not to overextend $h_{\max}$, as the model is only valid for $R \gg h$. The following logic is used to numerical differentiate the total capillary force given by Equation (44). The interval $[h_{\min}, h_{\max}]$ is divided into n-elements of equal size, with the distance at each consecutive step denoted by h_i (with $i \in \mathbb{N}$), and where n is the number of steps. The step size is

$$\Delta h = \frac{h_{\max} - h_{\min}}{n}. \tag{45}$$

The change in the capillary force at element i is the difference between the capillary force at separation distance h_i and one iteration later at $h_i + \Delta h$, such that

$$\Delta F_{\text{cap},i} = F_{\text{cap}}(h_i + h_{i+1}) - F_{\text{cap}}(h_i). \tag{46}$$

Thus, the stiffness of the capillary bridge at separation distance h_i is

$$k_{\text{c,i}} = \frac{F_{cap}(h_i + h_{i+1}) - F_{\text{cap}}(h_i)}{h_{i+1} - h_i}. \tag{47}$$

3.3 Ramping Experiment

3.3.1 Concept

The initial proposal was to coat the naturally hydrophilic (SiO_2) colloidal probe with OTS', to then wear the apex by sliding the probe onto a hard surface, revealing the hydrophilic area underneath (see Figure 15). The hypothesis was that the hydrophilic area would serve as a nucleation site for the condensation of a capillary bridge, while also providing a pinning area such that the capillary bridge would remain in place. The physical confinement of the hydrophilic area (by surrounding it by the hydrophobic OTS') would serve as an overflow barrier [25]. By decreasing the distance between the probe and the surface, the capillary bridge would overflow onto the hydrophobic portion of the probe, resulting in a convex capillary bridge and, hence, a repulsive capillary force. The wear procedure, however, was unsuccessful, as the toluene used for the OTS' solution affected the adhesive between the colloidal probe and cantilever, causing the colloidal probe to come loose rather easily.

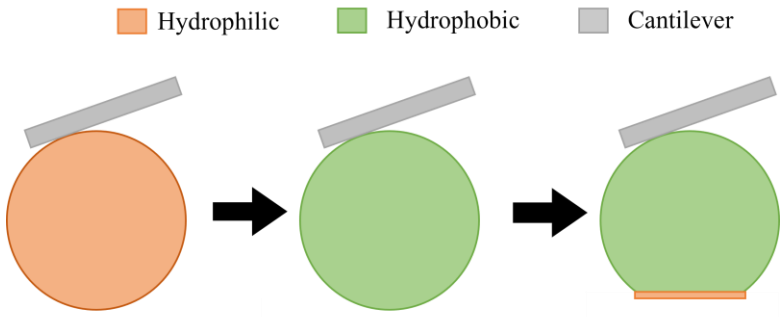

Figure 15: Schematic illustration of the initial concept. The colloidal probe (left), which is naturally hydrophilic, is coated with OTS' to make it hydrophobic (middle). The apex of the coated probe is worn off (right) by sliding it onto a hard surface, revealing the hydrophilic layer underneath.

Therefore, it was decided to conduct the ramping experiments with colloidal probes that were made super-hydrophilic (utilizing UV-Ozone treatment), and probes coated with the hydrophobic OTS'. The snap-in and pull-off forces were measured in a combination of different probe and wafer wettability, as is illustrated in Figure 16.

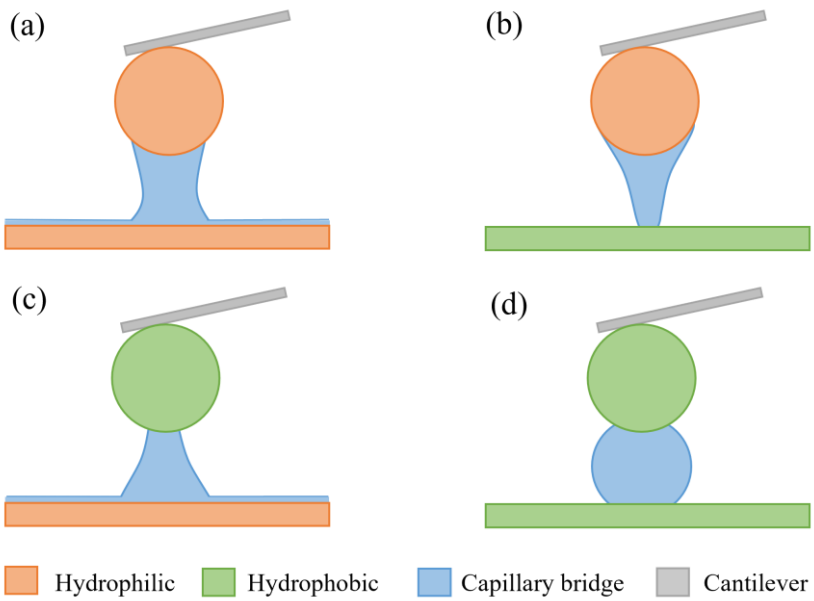

Figure 16: Schematic overview of the ramping experiments. (a) Shows a hydrophilic probe and hydrophilic wafer, (b) shows a hydrophilic probe and a hydrophobic wafer, (c) shows a hydrophobic probe and hydrophilic wafer, and (d) shows a hydrophobic probe and hydrophobic wafer. The size of the capillary bridges is drawn out of proportion for illustration purposes.

3.3.2 Experimental Setup

The ramping experiments were performed by using the Innova (Bruker) AFM.[2] The Innova is a compact AFM, capable of analyzing surface topography and force interactions at the nanoscale (specifications in Figure 38, Appendix III). Probes with two different spring constants were used, namely, k = 3 N·m^{-1} and k = 42 N·m^{-1}. Concerning the lab conditions, the relative humidity in the lab was maintained at 50%, and the temperature at 21 °C.

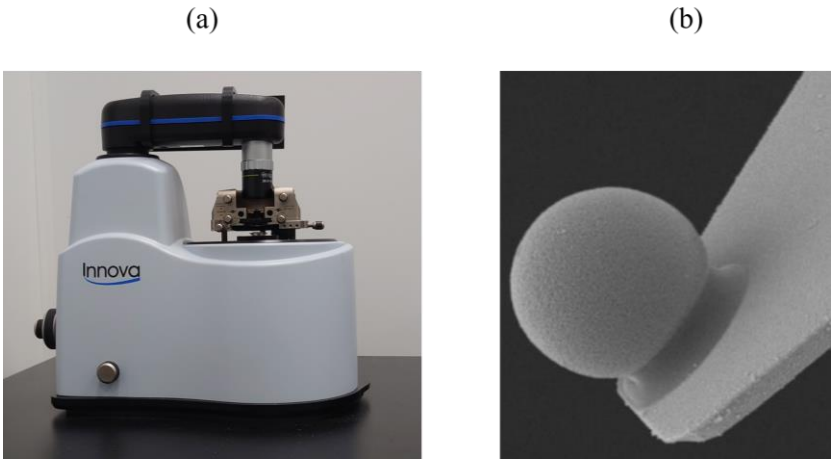

Figure 17: An image of (a) the Innova AFM and (b) a SEM image of the colloidal probe (diameter = 6.62 µm) used for the ramping experiments [26].

[2] If the reader wants know how the AFM operates, it is adviced to read through an overview provided by N. Ishida [28]. For digital readers, click the following link.

3.3.3 Execution

The measurements were performed by using the Nanodrive software (Bruker) in the Contact Mode. Initially, problems were encountered while performing test measurements. An oscillating motion was observed in the force-distance curves when approaching towards and retracting from the surface in the absence of a force, as is shown in Figure 35, Appendix II. This problem was solved by repositioning the laser to the middle of the cantilever, instead of the conventional positioning which is at the base of the apex (see Figure 36, Appendix II). This solution minimized the oscillation.

The Innova measures the deflection signal in Volts. Thus, before every set of measurements, the sensitivity of the cantilever was calibrated. Once calibrated, the deflection signal was set to Newton and the ramping experiments were conducted. Each set of measurements (see Figure 16 for reference) was repeated 10 times at an arbitrary spot on the wafer. The approach and retract speed were 5 $nm \cdot s^{-1}$. This relatively low movement speed was selected to ensure the condensation of a capillary bridge and to acquire a higher level of accuracy in the force-distance curves. After the measurements were completed, the NanoscopeAnalysis Software (Bruker) was used to process the data. The data were exported to text files and imported and organized in Excel. Afterward, the data analysis and visualization were done in Python.

3.4 Friction Force Experiment

3.4.1 Concept

For this experiment, the initial concept was to produce small (microscale) hydrophilic areas on an OTS' coated wafer. Microscopic water droplets would be deposited on the wafer by a nebulizer after which friction force experiments were to be conducted. The suggestion was that the hydrophilic areas would serve as pinning areas for the water molecules, thus keeping the droplets in place. Figure 18 shows an illustration of the concept.

Two methods were attempted to produce the hydrophilic areas. The first method involved covering the part of the wafer that was preferred to remain hydrophobic with aluminum foil, followed by UV-Ozone treatment. The part of the wafer that was left exposed turned hydrophilic because of the chemical reaction of the ozone with the organic OTS's, breaking the bonds that hold the molecule attached to the surface of the wafer. It is a relatively straightforward method to achieve local hydrophilicity. The drawback of this method, however, is the inability to accurately control the desired dimensions. The second method involved the removal of the coating through laser ablation. The laser ranging from low to high power was directed at the wafer at varying exposure times. The challenge was to find the laser power whereby the OTS's coating was removed without damaging the silicon underneath. However, it was found that the results were inconclusive, as is explained in Appendix I. Therefore, the friction force experiment was conducted with non-ablated hydrophobic wafers.

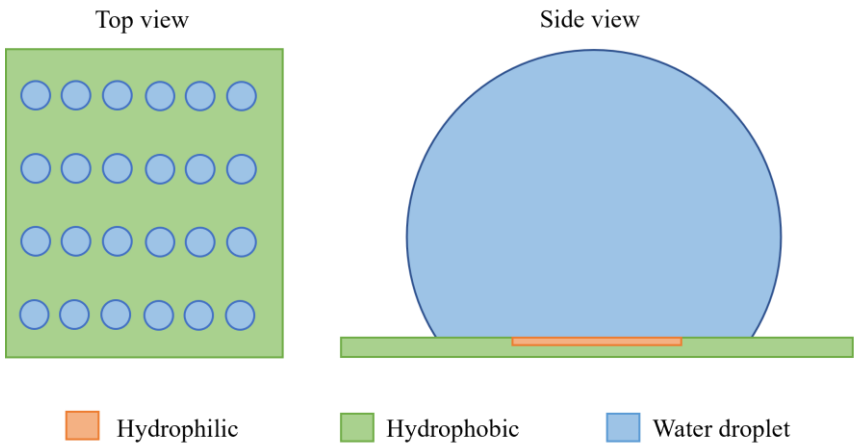

Figure 18: Schematic illustration of the initial concept. Hydrophilic areas of no more than a few hundred µm would serve as a pinning area for the microscopic water droplets, keeping them in place during the friction force experiment.

3.4.2 Experimental Setup

The friction force experiments were performed using the UMT TriboLab (Bruker) tribometer. The UMT is capable of measuring the friction force in the normal and lateral direction with high precision (specifications in Figure 38, Appendix III). For this experiment, only the force in the lateral direction was used. An overview of the experimental setup is shown in Figure 19.

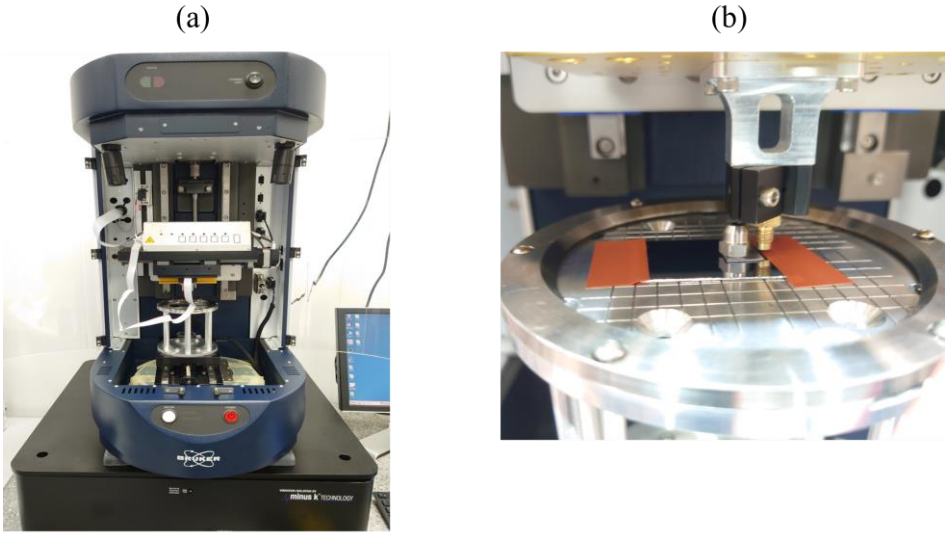

Figure 19: An image of (a) the UMT used for the friction force experiment, and (b) the experimental setup.

A schematic overview of the experiment is shown in Figure 20. Two types of modified wafers were used: a UV-Ozone treated superhydrophilic wafer and an OTS's coated hydrophobic wafer. The bottom wafer was attached to the stage plateau with tape. The larger size of the bottom wafer was to ensure that the top wafer had enough room to slide. A nebulizer (Medisana UHW, Medisana) was used to deposit water droplets onto both wafers. The weight placed on the top increased the normal load, thus increasing the friction force. The sensor had a force maximum of 5 N. By moving the sensor in the lateral direction, and subsequently sliding the top wafer over the bottom, the friction force was measured. The experiment was conducted in the following combinations: both wafers hydrophilic, both wafers hydrophobic, bottom wafer

hydrophilic and top wafer hydrophobic, and bottom wafer hydrophobic and top wafer hydrophilic. The weight had a mass of (1.7187±0.0001) gr, the hydrophobic top wafer a mass of (0.1684±0.000)1 gr, and the hydrophilic top wafer a mass of (0.1827±0.0001) gr. As with the previous experiment, the relative humidity in the lab was maintained at 50% and the temperature at 21 °C.

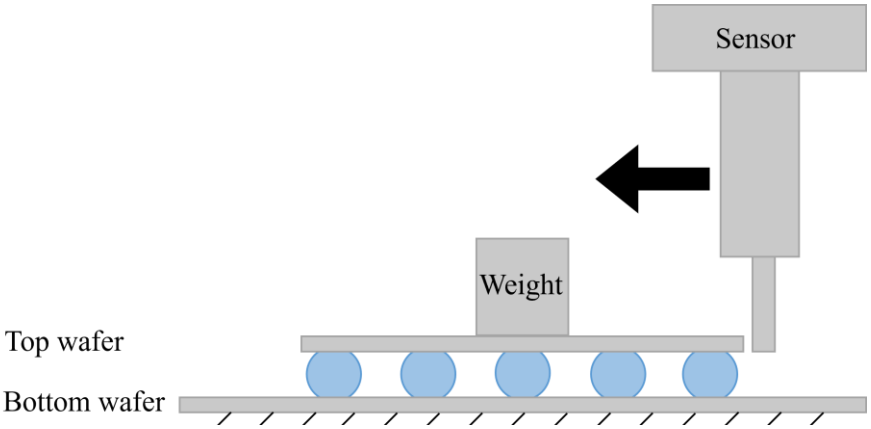

Figure 20: Schematic overview of the friction force experiment. Small water droplets are deposited on the surface using a nebulizer. The load is increased by the weight on the top wafer. The friction force is determined by sliding the top wafer over the bottom wafer.

3.4.3 Execution

The experiment was performed as follows. Microdroplets were deposited on both wafers using the nebulizer (see Figure 34, Appendix II). Once the sensor was positioned correctly, the system was calibrated by performing a calibration measurement. After the calibration, the friction force was measured. The sensor moved in the lateral direction with a speed of 1 mm·s^{-1} for a duration of 10 s. Every set of measurements was repeated five times to gather statistics. The data was exported to text files, after which it was imported and organized in Excel. Afterward, the data analysis and visualization were done in Python.

3.5 Uncertainty analysis

For the contact angle measurements, the statistical uncertainty was determined by the standard deviation. For the repulsive capillary force model, no error margin was incorporated. Concerning the ramping experiment, according to the datasheet, the Innova has an open-loop xy drift of < 1 nm·min^{-1}, and a closed-loop wy drift of < 3 nm·m^{-1}. Since each measurement took about 3 mins, the error in the z-position is assumed to be negligible. Moreover, it proved to be difficult to find an exact error margin on the sensor that measures the signal of the deflected laser. Since it is assumed that the statistical uncertainty of the measurements is greater than the systematical error, the standard deviation was used. Concerning the friction force experiments, the same obstacle was encountered. Therefore, the standard deviation was used as the statistical uncertainty.

4 Results and Discussion

4.1 Contact Angle Measurements

Figure 21 shows the results of the contact angle measurements on a stock silicon wafer (Figure 21.a), after treating the wafer with UV-Ozone (Figure 21.b), and after application of the OTS' coating (Figure 21.c). The contact angle θ_C on a stock silicon wafer is measured at (43±4)°, which is considered slightly hydrophilic. After treating the wafer with UV-Ozone, the contact angle decreased to <3°, rendering the surface highly hydrophilic, and indicating that an oxide layer of a few nm thick has grown on its surface [27]. Following the coating procedure, the contact angle on an OTS' coated silicon wafer was measured at (106±1)°. For conventional octadecyltrichlorosilane, literature reports a contact angle between 100 to 120°, depending heavily on how the procedure is performed [6, 7, 8]. Hence, it is concluded that in terms of wettability, the octyltrichlorosilane (OTS') performs as well as octadecyltrichlorosilane (OTS). The coating procedure that has been established is therefore regarded as valid. Moreover, since the probe is made of SiO_2 and the surface of the silicon wafer is naturally oxidized, a similar contact angle is assumed for an OTS' coated colloidal probe. However, the density distribution of the OTS' and its resistance to wear have not been investigated.

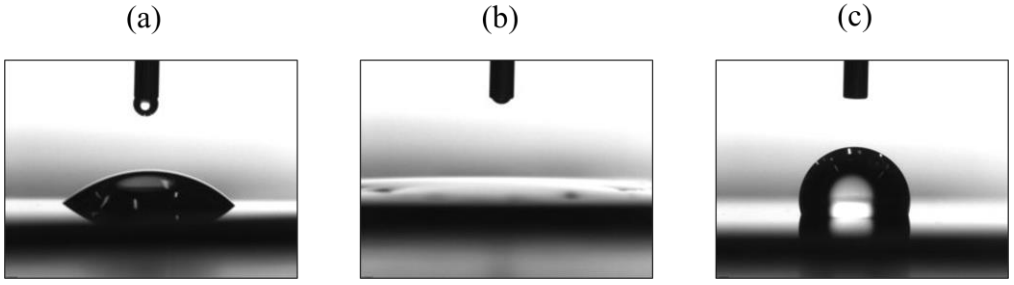

Figure 21: Images of the contact angle measurements. The contact angle θ_C is measured at (a) (43±4)° on a stock silicon wafer, (b) < 3° after treating with UV-Ozone (c) (106±1)° after applying an OTS coating. The results agree with previous results found in the literature.

4.2 Repulsive Capillary Force Model

To demonstrate the magnitude of capillary forces that can theoretically be expected, consider a capillary bridge as is illustrated in Figure 11. Equation (32) is used to calculate the tension force, Equation (33) for the Laplace force, Equation (34) for the total capillary force, and Equation 44) for the stiffness. The parameters include the contact angle θ_C, the volume of the capillary bridge V and the separation distance h between the two planar surfaces. For the surface tension, the value of water $\gamma = 72.75 \cdot 10^{-3}$ N·m^{-1} is used. Keep in mind that this model is merely theoretical and does not necessarily reflect the forces that can be observed in practice.

Firstly, an example is provided to give an idea of the interplay between the tension force, Laplace force, and the total capillary force. Consider a water droplet with a radius of 1 cm, equating to a volume of V of roughly 4.2 cm^3. For the sake of convenience, the effect of gravity in this example is negligible. The parameter θ_C is set to 110° and h is varied from a minimum of 0.01 mm to a maximum of 1 mm. Note that at a separation distance of 0.01 mm, the wetted radius $R \approx 365$ mm, and at a separation distance of 1 mm $R \approx 36.5$ mm, such that the condition $R \gg h$ is satisfied. The tension force, The Laplace force, and the total capillary force as a

function of the separation distance is shown in Figure 22. The Laplace force (Figure 22.a) shows a polynomial relationship that increases as the separation distance decreases. From Equation (23) it is evident that the Laplace force scales with R^2, while also scaling with the term $(1/r_1+1/r_2)$. As the separation height decreases, both R and r_1 increase, whereas r_2 decreases, resulting in an increase in the Laplace force. The tenson force (Figure 22.b) is negative and likewise exhibits a polynomial relationship, increasing as the separation distance decreases. From Equation (24) it is apparent that the tension force scales linearly with R, thus its contribution to the capillary force is significantly less when compared to the Laplace force. Consequently, the main contributor to the total capillary force (Figure 22.c) at relatively small separation distances is the Laplace force. Figure 22.d shows the normalized ratio of Laplace and tension force to the capillary force. At relatively small separation distances, the Laplace force dominates the tension force. As the distance increases, however, the contribution of the tension force increases until it exceeds the Laplace force, after which the capillary force changes from being repulsive to attractive. Due to limitations of the model, however, no attractive capillary force can be calculated. Nevertheless, attractive capillary forces at greater separation distances can be observed, as is described by more elaborate models by other authors [18].

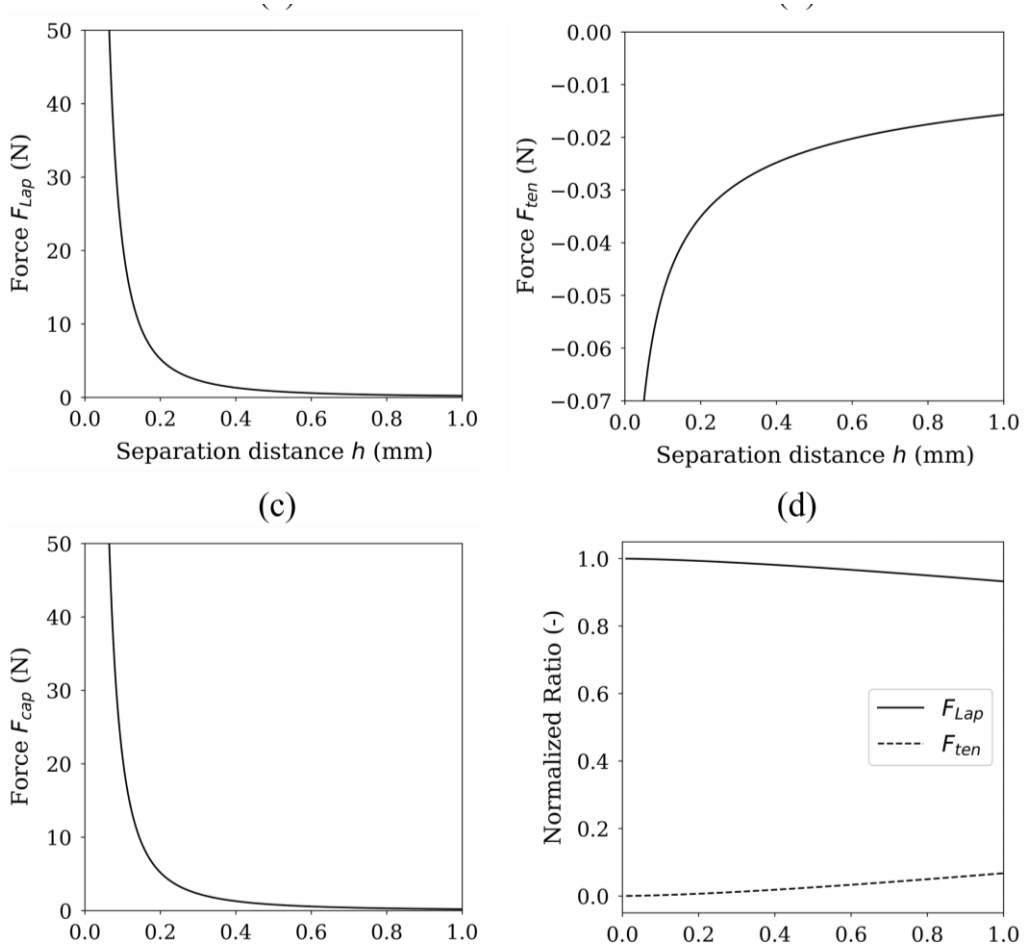

Figure 22: (a) The Laplace force, (b) the tension force, and (c) the total capillary force as a function of the separation distance h. (d) shows the normalized ratio of the Laplace force and tension force to the total capillary force.

Now that the interplay between the forces has been demonstrated, an analysis is presented regarding the magnitude of forces that can be expected on the micro and nanoscale. Consider, this time, a microscopical water droplet with a radius of 10 µm, equating to a volume of about $4.2 \cdot 10^3$ µm^3. The separation distance h is varied from a minimum of 10 nm to a maximum of 1000 nm. Three contact angles are set: $\theta_1 = 110°$, $\theta_2 = 130°$, and $\theta_3 = 150°$. Figure 23 shows the capillary force and stiffness as a function of the separation distance at contact angles θ_1, θ_2, and θ_3. At a separation distance of 10 nm, a single capillary bridge results in a repulsive capillary force in the order of 1 N and a stiffness in the order of 10^8 N·m^{-1}.

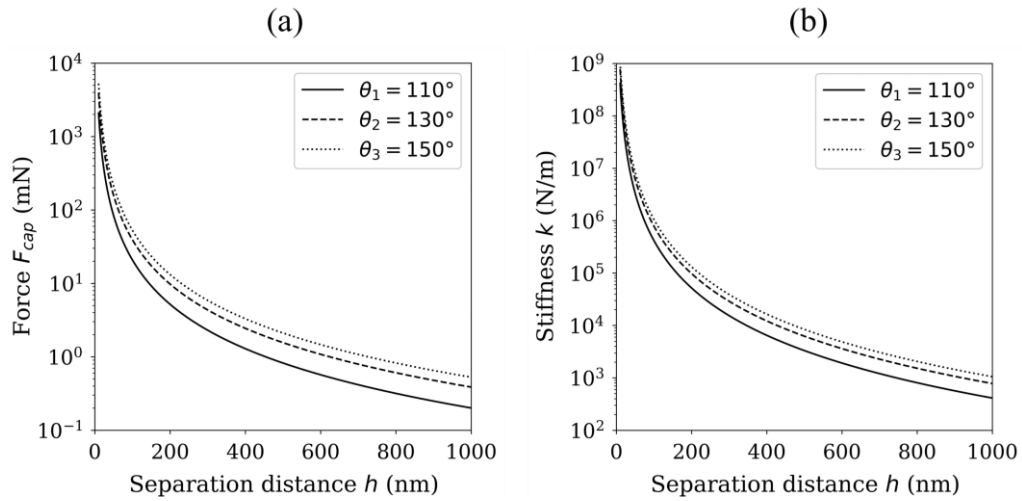

Figure 23: (a) The capillary force and (b) stiffness as a function of the separation distance at contact angles $\theta_1 = 110°$, $\theta_2 = 130°$, and $\theta_3 = 150°$. The graphs are displayed on a logarithmic scale.

Following the previous results, calculations are presented for the case where the contact angle is fixed at 110° and the volume is varied. The water droplet with a volume of $4.2 \cdot 10^3$ µm^3 is denoted as V^*, and the following three volumes are set: $V_1 = V^*$, $V_2 = 0.2V^*$, and $V_3 = 5V^*$. Figure 24 shows the capillary force and stiffness as a function of the separation distance at volumes V_1, V_2, and V_3. At a separation distance of 10 nm, a repulsive capillary force in the order of 0.1 to 1 N can be expected, and a stiffness in the order of 10^7 to 10^8 N·m^{-1}.

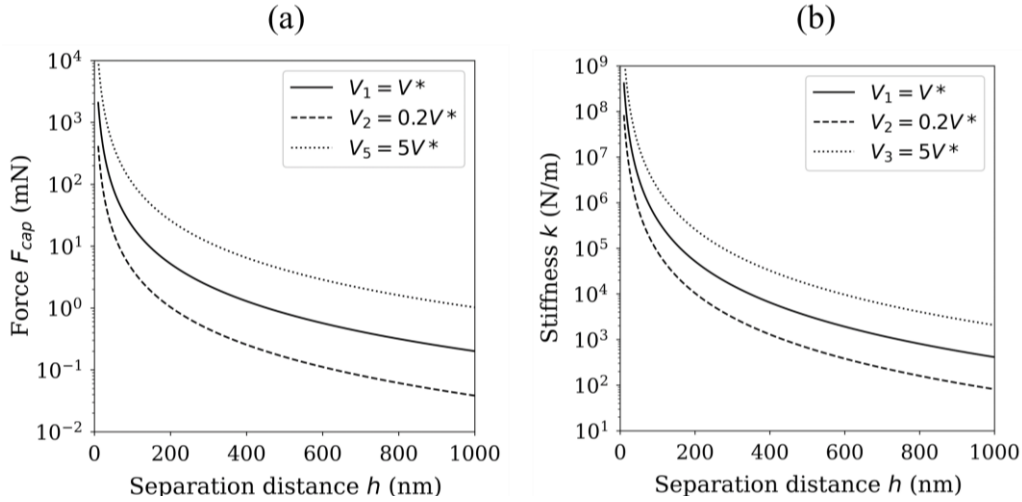

Figure 24: (a) The capillary force and (b) stiffness as a function of the separation distance at volumes $V_1 = V^*$, $V_2 = 0.2V^*$, and $V_3 = 5V^*$, where $V^* = 4.2 \cdot 10^3$ µm^3. The graphs are displayed on a logarithmic scale.

To summarize, for a fixed volume, a greater contact angle leads to a greater repulsive force and stiffness. Likewise, for a fixed contact angle, a greater volume results in a greater repulsive force and stiffness.

Lastly, to link theory to practice, a practical example of a water droplet between two hydrophobic OTS' coated wafers is shown in Figure 25. In Figure 25.a, the weight of the inclined top wafer is supported by the repulsive force that is exerted by the convex capillary bridge. In Figure 25.b, the convex profile of the capillary bridge is visible.

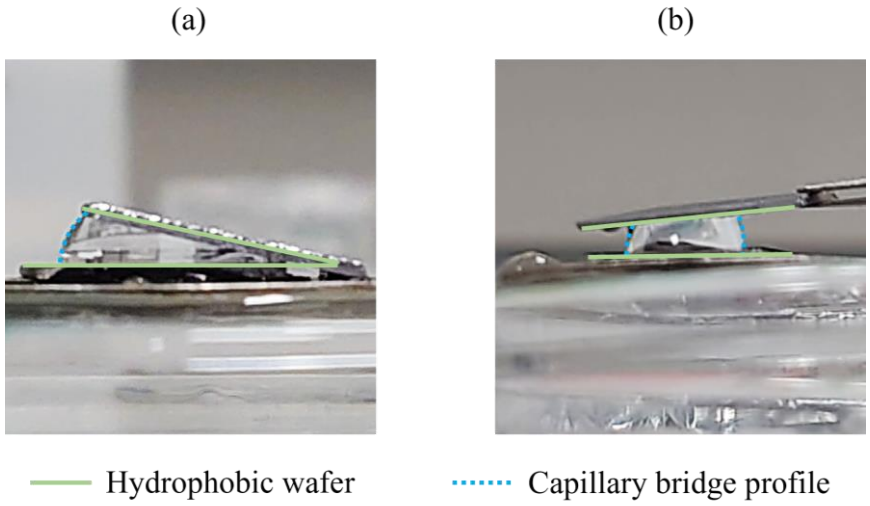

Figure 25: A picture of two hydrophobic OTS' coated silicon wafers with a water droplet in between. (a) The inclined top wafer is supported by the repulsion of the capillary bridge. (b) The convex profile of the capillary bridge. The contact angle of water on an OTS' coated silicon wafer is (106±1)°.

4.3 Ramping Experiment

For ease of readability, the notation in the following section is such that P = probe, W = wafer, subscript i = hydrophilic, and subscript o = hydrophobic.

A few selected force-distance curves for k = 3 N·m^{-1} are shown in Figure 26. For the case where $P_i + W_i$ and $P_i + W_o$, the snap-in and snap-off occurs instantly (Figure 26.a and b respectively) as a result of an attractive force caused presumably by a capillary bridge. Once the probe separates from the surface of the wafer, contact with the capillary bridge is immediately interrupted. The jump is a result of instabilities that occur only if the spring constant is lower than the slope of the interaction force along the separation distance [10, 28]. For $P_o + W_i$ and $P_o + W_o$ (Figure 26.c and d respectively), as the probe separates from the surface, a gradual decrease in the pull-off force is observed. One explanation for this trend implies that a capillary bridge is present between the probe and surface. For $P_o + W_i$, the retract curve can then be attributed to the evolution of the capillary bridge profile, where the sharp rise to zero indicates its breakpoint. For $P_o + W_o$, however, no capillary bridge is expected to be present since no water layers are assumed to be present on either surface. Alternatively, the trend for $P_o + W_o$ can attributed to a phenomenon called hydrophobic attraction. When two hydrophobic surfaces are in near contact and immersed in water, a concave air bridge may form, reason being that it is energetically favorable to replace the water with air [29]. The concave air bridge results in an attractive force, which may explain the gradual decrease in the retract curve. However, for $P_o + W_i$, the trend can not be explained by hydrophobic attraction.

Since no measurements were done to determine whether a water layer is present on the OTS' coated wafer or probe, further investigation is required.

The discrepancy between the magnitude of the pull-off force for $P_i + W_o$ and $P_o + W_i$ (Figure 26.b and c respectively) is unexpected as well. If the assumption that the wettability of the probe and wafer are equal (Section 4.1) is correct, a similar magnitude in the pull-off force is expected. The fact that they differ by about 400 nN is an indication that this assumption might not be true after al. Measurements to determine the contact angle of the UV-Ozone treated and OTS' coated probe should be conducted to provide clarification.

Lastly, no repulsive capillary forces have been observed as was initially expected for $P_o + W_o$ (see Section 3.3.1). Two possible explanations are discussed. Firstly, the size of a capillary bridge due to capillary condensation is in the order of nm, and the colloidal probe is 6.62 µm in diameter. Even if a repulsive force was present, its magnitude was most likely negligible when compared to the attractive van der Waals forces between the probe and surface. Another explanation is that, due to the sudden snap-in, capillary condensation had no time to commence.

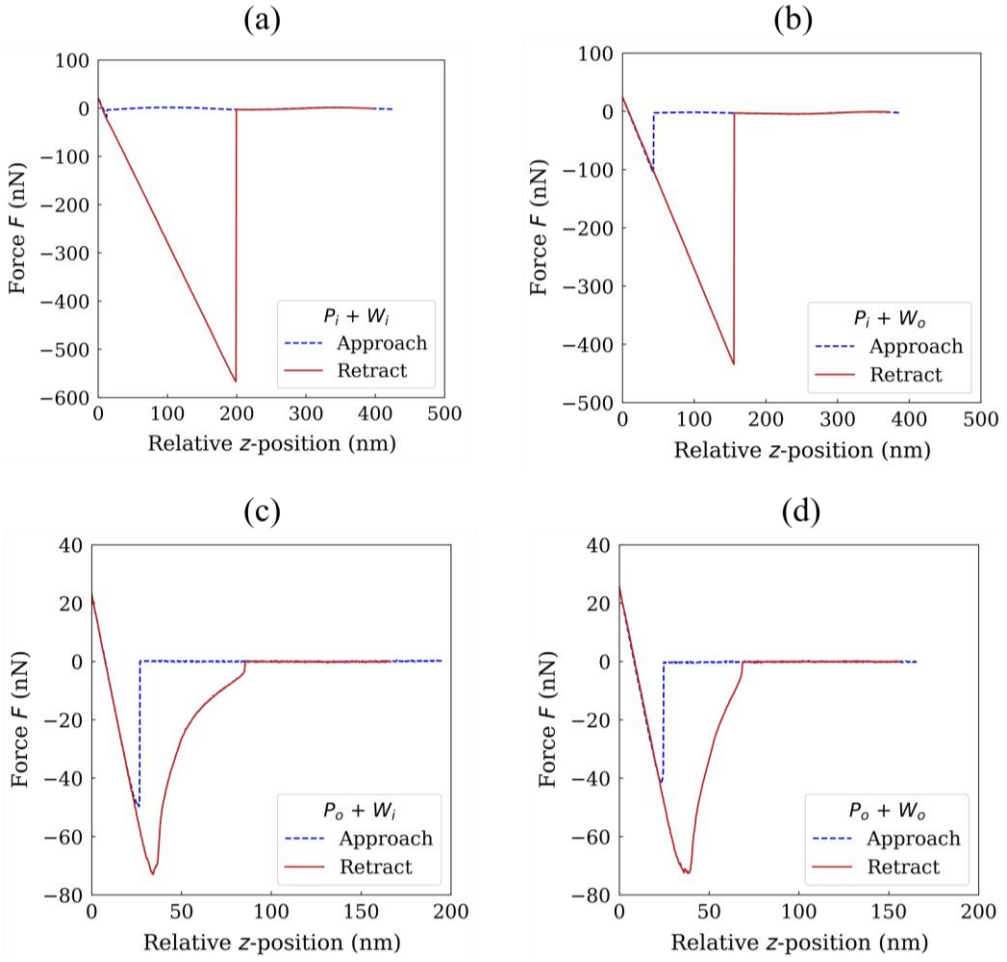

Figure 26: Force-distance curves of different combinations of probe and wafer wettability. The probe has a diameter of 6.62 µm and a spring constant of 3 N·m^{-1}. The curves are read as such: approach curve from right to left and retract curve from left to right.

A few selected force-distance curves for k = 42 N/m are shown in Figure 27. For $P_o + W_i$ and $P_o + W_o$ (Figure 27.c and d respectively), during the approach, the curve shows a slight jump, followed by a gradual increase in the snap-in force until hard contact with the surface is made. When compared to the previous results, the higher spring constant prevents the probe from immediately snapping onto the surface. It is suggested that the probe pushes into presumably a water layer, present on both the hydrophilic and hydrophobic surfaces. The discrepancy between the approach curve for $P_o + W_i$ and $P_o + W_o$ indicates a thicker water layer for a hydrophilic surface, and a thinner layer for the hydrophobic surface. For the retract curve, a gradual decrease in the adhesion force is noticeable as the separation distance increases. This is an indication that, again, that the evolution of the capillary bridge profile is visible.

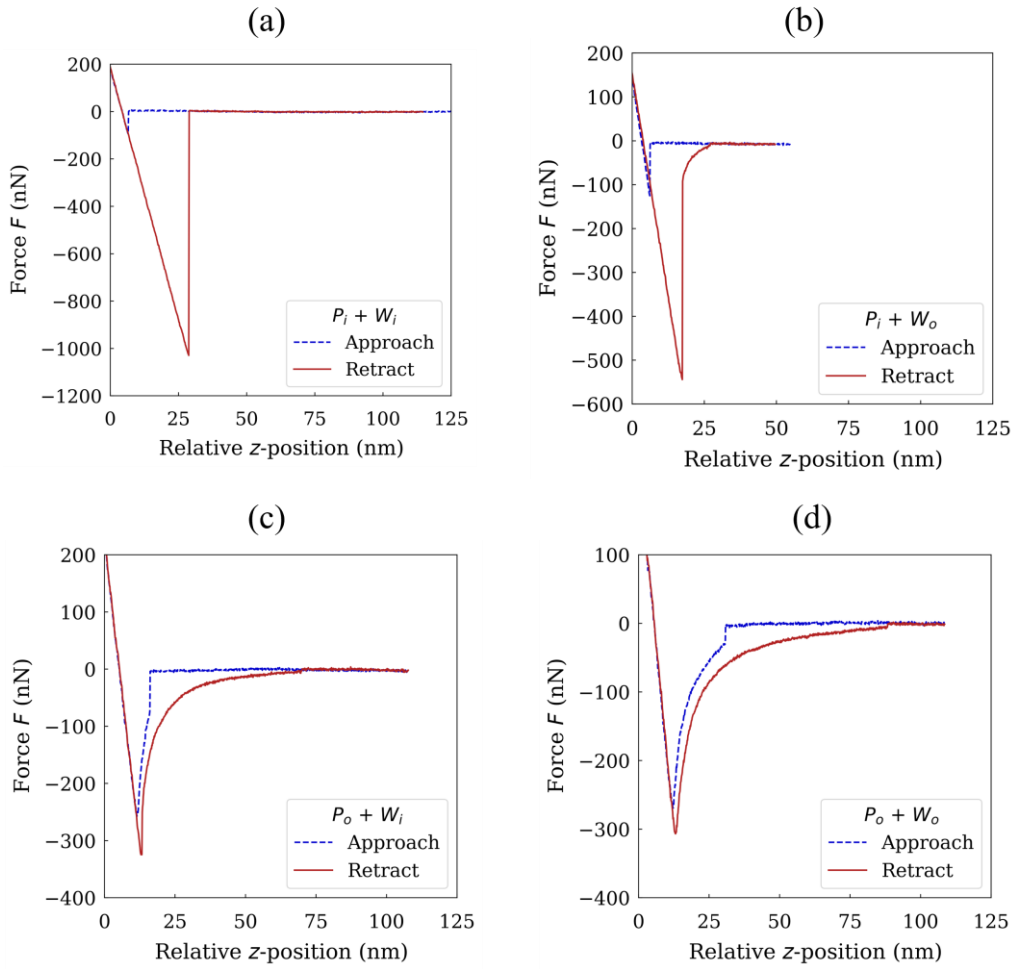

Figure 27: Force-distance curves of different combinations of probe and wafer wettability. The probe has a diameter of 6.62 µm and a spring constant of 42 N/m. The curves are read as such: approach curve from right to left and retract curve from left to right.

Figure 28 shows an overview of the snap-in and pull-off forces for different combinations of the probe and wafer wettability (Figure 28.a for k = 3 N·m^{-1}and Figure 28.b for k = 42 N·m^{-1}). Consider Figure 28.a. For $P_i + W_i$, the pull-off force is relatively high and can be attributed to the strong attractive capillary force. The highest snap-in force was expected in for this case, as a water layer is assumed to be present on both hydrophilic surfaces. This should, in theory, result in a relatively early snap-in distance and, hence, a relatively high snap-in force. However, the lowest snap-in force of any of the cases is observed. The mechanism responsible for this

phenomenon is yet to be understood. For $P_o + W_o$, a significant decrease in the pull-off force is observed, indicating that the contribution of the capillary force to the adhesive force is significantly reduced. In addition, the pull-off force is an indication of the strength of the attractive van the van der Waals forces between the probe and wafer since no capillary bridge is assumed to be present. As mentioned before, the higher pull-off force when compared to the snap-in force is due to the instability of the probe. Furthermore, when comparing $P_i + W_o$ to $P_i + W_i$, the pull-off force decreased, while the snap-in force increased. The decrease in pull-off force can be attributed to the weaker attractive capillary force. The increase in the snap-in force, however, contradicts that, suggesting a stronger attractive capillary force. For $P_o + W_i$, the snap-in and pull-off force are comparable to $P_o + W_o$. When considering Figure 28.b, the same trend in the pull-off force is observed. The snap-in force shows an increase from left to right, where a decrease is expected for the same reason as mentioned before. The discrepancy between the magnitude of the overall snap-in and pull-off forces between the probes with k = 3 N·m^{-1} and k = 42 N·m^{-1} is most likely due to the unconventional laser alignment, as is described in Section 3.3.3. This may have resulted in different calibrated sensitivities, which leads to different measured forces.

A considerable reduction in pull-off force is observed when comparing $P_o + W_o$ to $P_i + W_i$. For k = 3 N·m^{-1}, the pull of force is reduced by 90%, and for k = 42 N·m^{-1}, the reduction is 68%. However, no repulsive capillary forces for $P_o + W_o$ have been observed, most likely due to the relatively small size of the capillary bridge that has formed, if any had formed. It must be noted that the results that are presented serve as preliminary, as conditions like RH and probe size dependency on the capillary force have not yet been investigated. To provide a more convincing explanation for the observed phenomena, further investigation is needed.

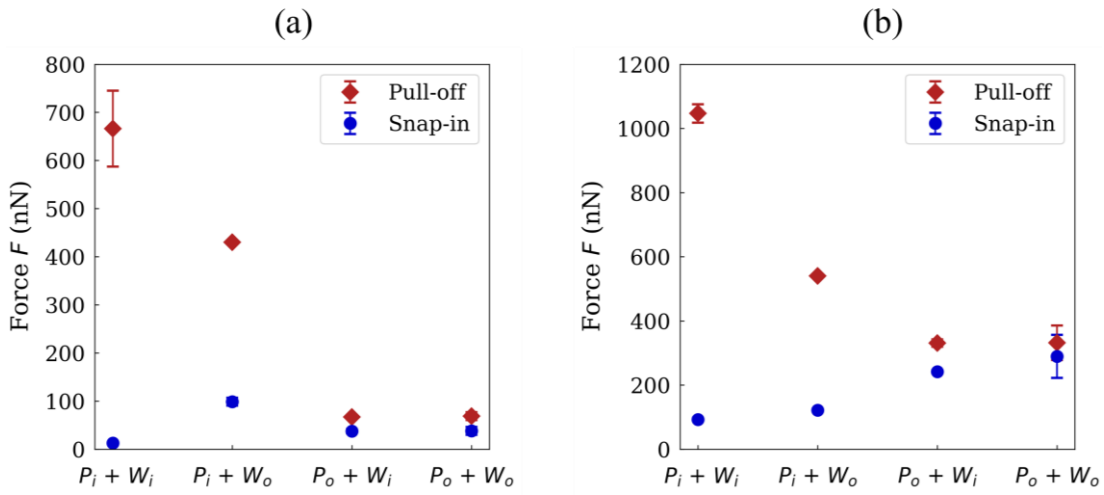

Figure 28: The snap-in and pull-off force for different combinations of probe and wafer wettability. (a) A probe with a spring constant of 3 N·m^{-1}and (b) a probe with a spring constant of 42 N·m^{-1}. The x-labels are labeled such that P = probe, W = Wafer, subscript i = hydrophilic and subscript o = hydrophobic.

4.4 Friction Force Experiment

For ease of readability, the notation in the following section is such that B = bottom wafer, T = top wafer, subscript i = hydrophilic, and subscript o = hydrophobic.

Figure 29 shows the friction force for the different combinations of wafer wettability. For $B_i + T_i$, the relatively high friction force is attributed to the strong attractive force of the capillary bridges. Comparing $B_o + T_o$ to $B_i + T_i$, a significant reduction of 99% in the friction force is observed. The reduction can be attributed to due to repulsive force of the capillary bridges, reducing the adhesion force and, hence, the friction force. The friction force for $B_o + T_o$ and $B_o + T_i$ are equal, where a lower force is expected for $B_o + T_i$ due to the attractive capillary force that is anticipated. Comparing the different combinations, however, is ambiguous, as precise control over the amount and volume of water droplets deposited on the surface was lacking. Although the wettability of each wafer type is assumed to be identical, the magnitude of capillary force, whether attractive or repulsive, depends on the amount of water that is present on each surface. For example, when comparing $B_i + T_o$ to $B_o + T_i$, a larger amount of water between one or the other results in a greater capillary force, even if the wettability of each wafer type is equal. However, since the experiment lack good statistics, and conditions like RH dependency and sliding velocity have not been investigated, further research is required.

Typically, Equation (45) is used to calculate the friction coefficient. However, since the magnitude of the adhesion force is unknown, this determining the friction coefficient proved to be impossible. Furthermore, it can be noticed that the friction force results follow the same trend as the ramping results (see Figure 28). Further investigation is needed to determine whether there is a correlation between the two.

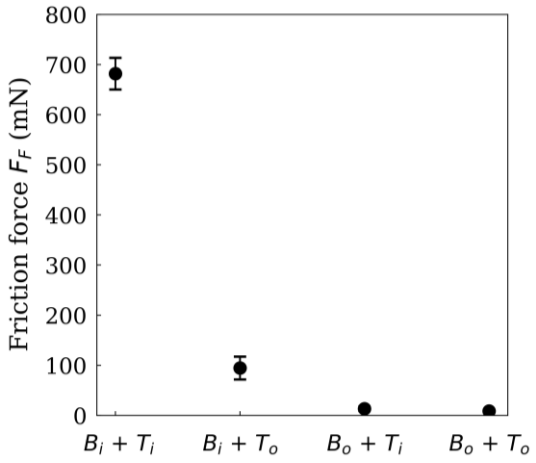

Figure 29: (a) The friction force at different combinations of wafer wettability. (b) The calculated friction coefficient μ. The x-labels are labeled such that B = Bottom, T = Top, subscript i = hydrophilic and subscript o = hydrophobic.

5 Conclusion

In this work, repulsive capillary forces are investigated to provide an insight into its mechanics and effects. On the theoretical side, a mathematical model has been developed for a capillary bridge between two planar solids with equal contact angles. This model can be used to calculate the capillary force and the stiffness in the normal direction to the planar surfaces, given the volume of the capillary bridge, the contact angle, and the separation distance between the two surfaces. For a microscopic water droplet with a radius of 10 µm, repulsive forces in the order of 1 N, and stiffness values in the order of 10^8 $N \cdot m^{-1}$ can theoretically be expected. For a given volume of water, the magnitude of the capillary force and stiffness increases at greater contact angles. Likewise, for a given contact angle, the capillary force and stiffness increase as the volume increases. In any case, both the capillary force and stiffness increase as the separation distance decreases. Due to limitations of the model, however, the calculations are only valid when the separation distance is relatively small when compared to the volume of the liquid.

On the experimental side, a procedure has been established for the coating of silicon wafers and silicon dioxide colloidal probes with a hydrophobic self-assembled monolayer. While most literature reports the use of octadecyltrichlorosilane as a coating substance, for this research, the closely related octyltrichlorosilane is utilized. The contact angle of water on the octyltrichlorosilane coated silicon wafer is measured at $(106 \pm 1)°$, which is in agreement with what literature reports on octadecyltrichlorosilane.

Atomic force microscopy has been employed to measure the adhesion force between a colloidal probe and a silicon wafer. The observed adhesion force between the hydrophobic probe and wafer is significantly reduced when compared to the hydrophilic combination, indicating that the influence of the attractive capillary force is significantly diminished. For the probe with a spring constant of 3 $N \cdot m^{-1}$, the pull-off force is reduced by 90%, and for the probe with spring a constant of 42 $N \cdot m^{-1}$, a 68% reduction in the pull-off force is measured. However, repulsive capillary forces have not been observed, possibly due to the relatively small size of the condensed capillary bridge compared to the size of the colloidal probe. It is theorized that the magnitude of the van der Waals force between the probe and surface is considerably greater than the repulsive force caused by the capillary bridge. Moreover, clarification of the observed phenomena is difficult, as the conditions in which the experiments were conducted were limited, and the measurements lack good statistics. Further investigation is required to interpret the results with more confidence.

The friction force has been measured between a combination of hydrophilic and hydrophobic wafers with water droplets deposited in between using a tribometer. For two hydrophilic wafers, a significant friction force is observed due to the strong attractive capillary force. On the contrary, for two hydrophobic wafers, a decrease of 99% in the friction force is observed, which is attributed to the repulsive force of the capillary bridges. In this case, the water droplets act as a kind of flexible ball bearing, rendering the water a good lubricant. The experiments, however, have been tested in too few conditions, and lack good statistics. To better understand the implications of the results, further research is required.

6 Recommendations

In the following section, a few recommendations are provided for any future experiments. Firstly, the integrity of OTS' coating needs to be examined. On a macroscopic scale, the measured contact angle seems to indicate that the coverage of the OTS' is homogenous. At the nanoscale, however, this is not the case, as the density distribution of OTS' varies throughout the surface. As the hydrophobicity on one particular location on the wafer can differ from another, the adhesion force will differ as well. Moreover, it is advised to investigate the wear resistance of the coating. Yet, it is unclear if the OTS' remained on both the probe and silicon wafer during the ramping experiments. Literature reports the possibility of pattern transfer to occur if the applied load is too great [8]. Furthermore, it was assumed that the wettability of the OTS' coated probe was equal to that of the silicon wafer. However, since this has not been verified, it remains an assumption. Difference wettability could explain the difference observed in the pull-off force between the hydrophobic probe and hydrophilic wafer, and the hydrophilic probe and hydrophobic wafer. Lastly, a method must be devised to wear the colloidal probe, such the OTS' coating is removed and the naturally hydrophilic SiO_2 underneath is revealed.

The ramping experiments were conducted under too few conditions, as literature report dependencies like relative humidity and probe size on adhesion force. To investigate whether repulsive forces can be observed with the AFM, utilizing a single asperity tip (tip radius of several tens of nm) is advised. Then, the size of the tip is in the same order as the size of a capillary bridge that condenses, thus increasing the likelihood that the repulsive capillary forces and van der Waals forces between tip and surface are in the same order of magnitude. Moreover, it is recommended that the experiments are repeated a great number of times and compared to different locations on the wafer to gather satisfactory statistics.

Likewise, the friction force experiments have been conducted under few conditions and lack statistics. It is recommended to devise a way to have more control over the amount and size of water droplets deposited on the surface, as that governs the magnitude of capillary force, whether attractive or repulsive. The friction force could also be investigated as a function of relative humidity. In this way, it is ensured that a (more or less) even amount of water is condensed between each surface. Moreover, since the friction force is dependent on the sliding velocity, velocity-dependent friction force experiments are recommended.

Furthermore, a method to produce small hydrophilic pockets on a hydrophobic wafer must be established. By treating the OTS' coated wafer with UV-Ozone, it is concluded that the wettability of the wafer changes from hydrophobic to hydrophilic. This method, however, lacks precise control over the desired dimensions. Alternatively, the desired effect can be produced by employing lithography. Using lithography, O. Kaspar et al. produced arrays of alternating hydrophobic/hydrophilic layers with microscopical dimensions [25]. If successful, the pinning effect of water could also be investigated.

Lastly, if a greater repulsive capillary force and stiffness are desired, micro-patterns can be introduced to the silicon wafer to enhance the hydrophobicity of the OTS' coating. Y. Song et al. reported an increase in contact angle from 112 to 155° on an OTS coated micro-patterned surface [30]. As is clear by now, a greater contact angle results in a greater capillary force and stiffness.

References

[1] L. Sirghi et al., "Volume of a Nanoscale Water Bridge," Georgia Institute of Technology, Atlanta, 2005.

[2] "Our Mission," ARCNL, [Online]. Available: https://arcnl.nl/our-mission#about. [Accessed 2021 08 19].

[3] G. Hornyak et al., Introduction to Nanoscience & Nanotechnology, Boca Raton: Taylor & Francis Group, 2009.

[4] P. de Gennes et al., Capillarity and wetting phenomena: Drops, Bubbles, Pearls, Waves, New York: Springer-Verlag New York, Inc, 2004, p. 23.

[5] P. Lambert, "Surface Tension in Microsystems: Engineering below the capillary length," Springer, Brussels, 2013.

[6] B. Arkles, Hydrophobicity, Hydrophilicity and silane surface modification, Morrisville: Gelest inc, 2011.

[7] K. Cha and D. Kim, Investigation of the tribological behavior of octadecyltrichlorosilane deposited on silicon, Shinchondong: Elsevier, 2001.

[8] S. Ren et al., "Friction and wear studies of octadecyltrichlorosilane SAM on silicon," Springer, 2002.

[9] S. Shoell et al., "Multifunctional SiC Surfaces: From Passivation to Biofunctionalization," Elsevier, 2012.

[10] J. N. Israelachvili, Intermolecular and Surface Forces, Amsterdam: Elsevier, 2011, p. 456.

[11] H. Nasrallah, "Capillary adhesion and friction: an approach with the AFM circular mode," Université du Maine, 2011.

[12] Y. Jin et al., "Atmospheric Water Harvesting, Role of Surface Wettability and Edge Effect," WILEY-VCH Verlag GmbH & Co. KGaA, Weinheim, 2017.

[13] L. Chen et al., "Water Absorption on Hydrophilic and Hydrophobic Surfaces of Silicon," The American Chemical Society, Washington D.C., 2018.

[14] E. Riedo and et al., "Kinetics of Capillary Condensation in Nanoscopic Sliding Friction," Physical Review Letters, 2002.

[15] M. Bazrafshan et al., "Adhesive force model at a rough interface in the presence of thin water films: the role of relative humidity," Elsevier, 2018.

[16] X. Xiao and et al., "Investigation of Humidity-Dependent Capillary Force," American Chemical Society, Hong Kong, 2000.

[17] M. He et al., "Critical phenomena of water bridges in nanoasperity contacts," University of Washington, Washington, 2001.

[18] B. Bhushan and S. Cai, "Meniscus and viscous forces during separation during separation of hydrophilic and hydrophobic smooth/rough surfaces with symmetric and asymmetric contact angles," The royal society, Columbus, 2008.

[19] Y. Wang et al., "Symmetric and Asymmetric Capillary Bridges between a Rough Surface and a Parallel Surface," Langmuir, Raleigh, 20.

[20] L. Yang and et al., "Capillary-bridge Forces Between Solid Particles: Insight from Lattice Boltzmann Simulations," Helmholtz Institute, Nürnberg, 2020.

[21] D. Megias-Alguacil and L. J. Guackler, "Analysis of the capillary forces between two small solid spheres binded by a convex liquid bridge," Elsevier, Zürich, 2009.

[22] N. Nguyena et al., "Theoretical and experimental study of capillary bridges between two parallel planes," European Journal of Environmental and Civil Engineering, Enschede, 2020.

[23] M. Bartosik et al., "Nanometer-Sized Water Bridge and Pull-Off Force in AFM at Different Relative Humidities: Reproducibility Measurement and Model Based on Surface Tension Change," ASC Publications, Purkyňova, 2016.

[24] F. Baumgart, "Stiffness - an unknown world of material science?," Elsevier, Clavadelerstrasse, 2000.

[25] O. Kaspar et al., "Confinement of Water Droplets on Rectangular Micro/Nanoarrayed surfaces," The Royal Society of Chemistry, 2013.

[26] "AFM Probe," NanoAndMore, [Online]. Available: https://www.nanoandmore.com/AFM-Probe-CP-CONT-SiO. [Accessed 17 08 2021].

[27] R. Williams and M. Goodman, "Wetting of thin films of SiO2 by water," Applied physics letter, 1974.

[28] N. Ishida and V. S. J. Craig, "Direct Measurements of Interaction Forces Between Surfaces in Liquids Using Atomic Force Microscopy," J-Stage Advance, Okayama, 2018.

[29] H. Christenson and P. Claesson, "Direct measurements of the force between hydrophobic surfaces in water," Elsevier, 2001.

[30] Y. Song et al., "Superhydrophobic Surfaces Produced by Applying a Self-Assembled Monolayer to Silicon Micro/Nano-Textured Surfaces," Springer, 2008.

[31] Bruker, "Innova AFM," [Online]. Available: https://www.bruker.com/en/products-and-solutions/microscopes/materials-afm/innova-afm.html. [Accessed 25 08 2021].

[32] Bruker, "UMT TriboLab," [Online]. Available: https://www.bruker.com/en/products-and-solutions/test-and-measurement/tribometers-and-mechanical-testers/umt-tribolab.html. [Accessed 27 08 2021].

Appendix I: Laser Ablation Experiment

The concept for the laser ablation experiment is described in Section 3.4 (see Figure 18). By irradiating the OTS' coated wafer with a laser, it was anticipated that the induced heat would, at a certain power and exposure time, break the bonds that hold OTS' molecules attached to the silicon wafer, revealing the hydrophilic silicon dioxide underneath. However, as mentioned in the main body of this work, the attempt to produce small hydrophilic areas on an OTS' coated wafer did not succeed.

II.A Experimental Setup

The laser ablation experiment was conducted by utilizing an in-house laser with a wavelength of 1064 nm and a pulse rate of 100 pulses/sec. Different exposure times were set by varying the number of pulses, and the spot size was set to 500 μm. An overview of the setup is displayed in Figure 30. The OTS' coated wafer was mounted in a special holder inside a vacuum chamber. However, it was decided not to put the chamber in a vacuum. The energy meter was used to calibrate the laser intensity. The laser was directed at a mirror, which in turn redirected the beam to the wafer. Since the OTS' coating is transparent and the wafer itself is reflective, the back-reflection power signal was measured using a power meter that was linked to a computer. The progression of the back-reflected signal was recorded by the computer used to verify if the ablation was successful. The hypothesis was that a decrease in back-reflected power would indicate if physical damage was done to the wafer, potentially removing the OTS' coating in the process. The challenge was to find the required power and exposure time, where the OTS' coating was removed without excessively damaging the wafer.

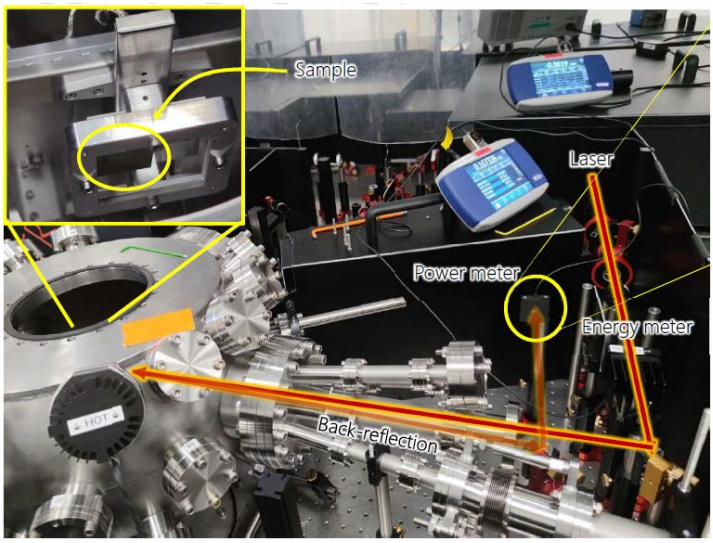

Figure 30: Overview of the laser setup. The laser was directed at a mirror, such that the beam was redirected to the OTS' coated silicon wafer. The back-reflection signal was in turn redirected by a mirror to a power meter that was linked to a computer.

II.B Execution

The ablation was done in four rows of varying laser power and exposure times, as is illustrated in Figure 31. First, a test experiment was done to find the range of laser power suitable to achieve the desired effect. It was concluded that a power ranging from 30 to 45 mW would be appropriate, with intervals of 5 mW. Afterward, four identifier spots at 200 mW were produced at the start of each row that would serve as markers. Hereafter, at each laser power, spots were

ablated in intervals of increasing exposure time, ranging from 1s to 200s. Subsequently, to examine whether the wettability of the ablated spots was affected, ramping experiments were conducted. Here, the pull-off force was measured on the ablated spots and the surrounding non-ablated area. The ablated spots were optically identified using the microscope of the Innova.

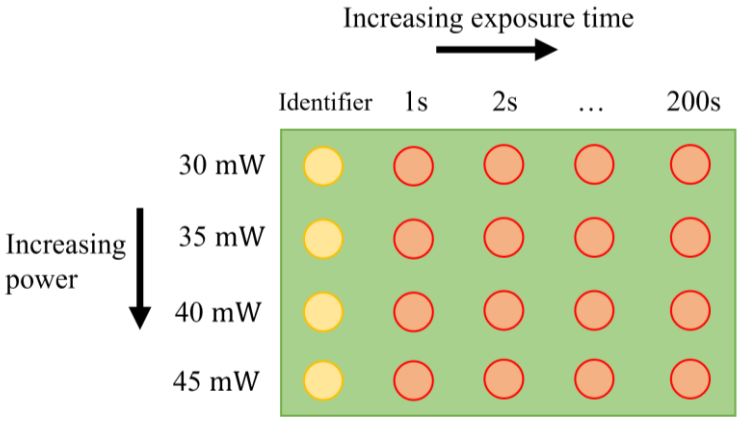

Figure 31: Overview of the laser ablation experiment of an OTS' coated silicon wafer (green). The identifier spots (yellow) serve as markers. For the ablation of the spots (red), the laser power varied from 30 mW to 45 mW at exposure times ranging from 1 to 200 seconds.

Pull-off test measurements on visibly damaged spots revealed an increase in hydrophobicity, the exact opposite of what was desired (see Figure 37, Appendix II). Moreover, it proved to be difficult to find the spots where little damage was done to the wafer, as those spots left no visible markers. Therefore, it was decided to use a nebulizer to deposit microdroplets on the wafer, for the purpose of condensing the droplets onto the hydrophilic spots. Consequently, residue was left behind in the ablated spots after the droplets evaporated, which made it easier to optically identify their position.

II.C Results

Figure 32 shows the reflection power P_r as a function of the exposure time t_e. For overview purposes only the results with the longest exposure times are shown. At 30.2 mW, the reflection power shows a negligible decrease over time, suggesting no physical damage to the wafer is done. At 35 mW, a slight decrease over time is observed, indicating that some damage was done. The progression of the reflection power at 40.2 mW is stable at first but decreases as the exposure time increases. At 45.1 mW, the reflection power decreases sharply almost immediately. At both 40.2 and 45.1 mW, the damage done to the wafer was optically visible using the microscope, even at short exposure times.

Figure 33 shows the pull-off force at a few selected spots that were identified after the evaporation of the droplets. Contrary to what was expected, the pull-off force on ablated spots is significantly lower than the surrounding OTS's coated area. This indicates, again, that the hydrophobicity increased instead of decreased. The pull-off force on a random spot (where residue was left behind, but no ablation had taken place) also shows a decrease when compared to its surrounding area. The suggestion is that, somehow, this residue affects the wettability of the surface, enhancing the hydrophobicity. Further investigation is required to find the origin of the increase in hydrophobicity. Therefore, the attempt to produce small hydrophilic areas by ablating the OTS' coating away is deemed unsuccessful.

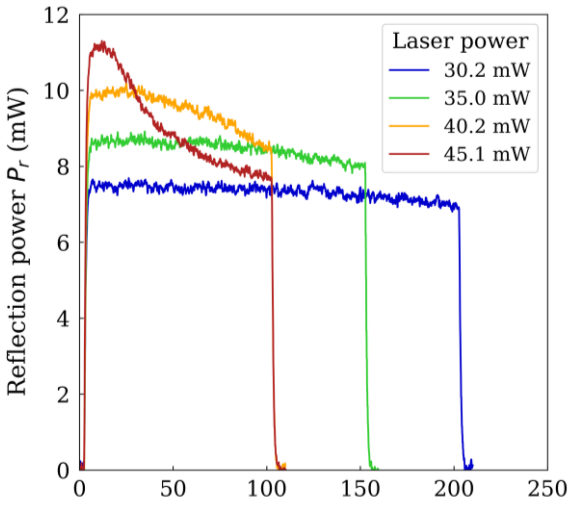

Figure 32: The reflection power as a function of the exposure time. At 30.2 and 35.0 mW, only a slight decrease in the reflection power over time is observed. At 40.2 and 45.1 mW, the reflection power decreases more sharply and occurs at relatively short exposure times.

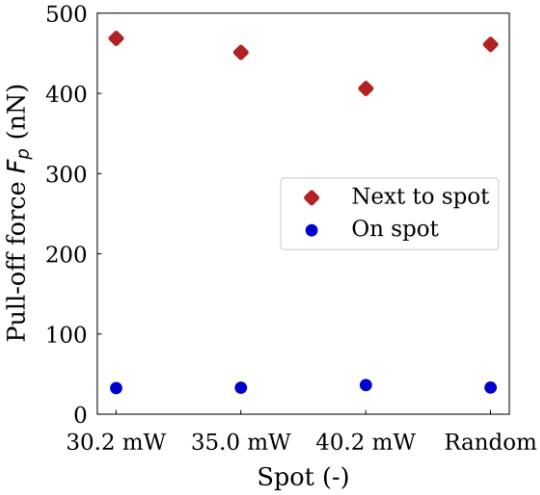

Figure 33: The pull-off force at the laser-ablated spots and surrounding OTS' coated area after depositing microdroplets on the wafer. The ablated spots show a significant decrease in pull-off force when compared to the surrounding OTS' coating.

Appendix II: Additional Figures

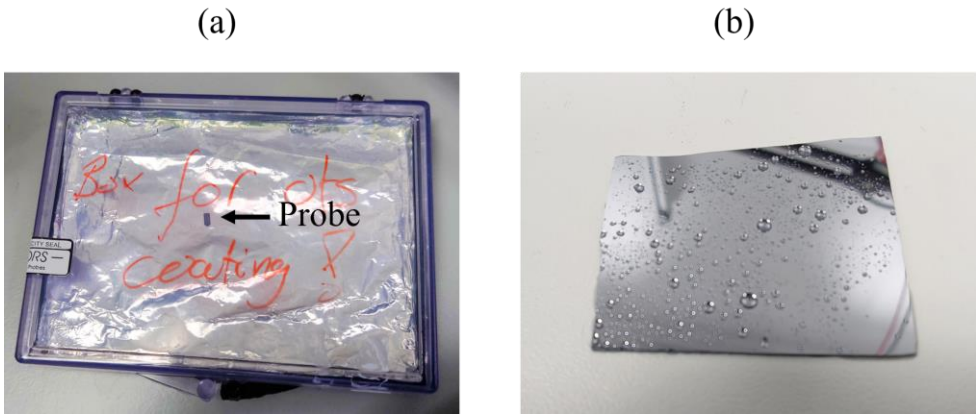

Figure 34: (a) Picture of a colloidal probe in a casing. The interior of the casing is covered with aluminum to prevent the OTS' reacting with the plastic walling. (b) Picture of water droplets deposited on an OTS' coated wafer.

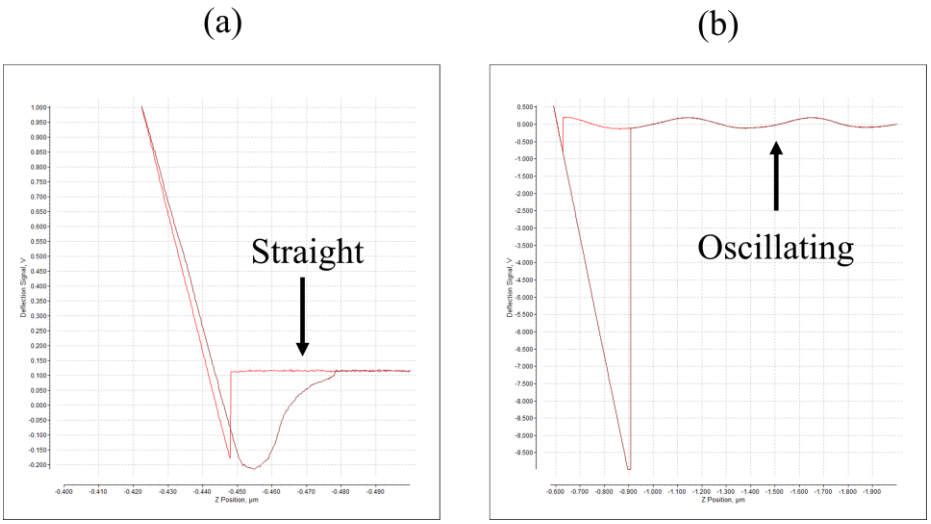

Figure 35: The approach and retract curve of (a) a single asperity tip and (b) a colloidal probe. (a) In the absence of a force acting on the probe, the approach and retract curves are practically straight. (b) An undesirable oscillating motion in the approach and retract curve is present in the absence of a force.

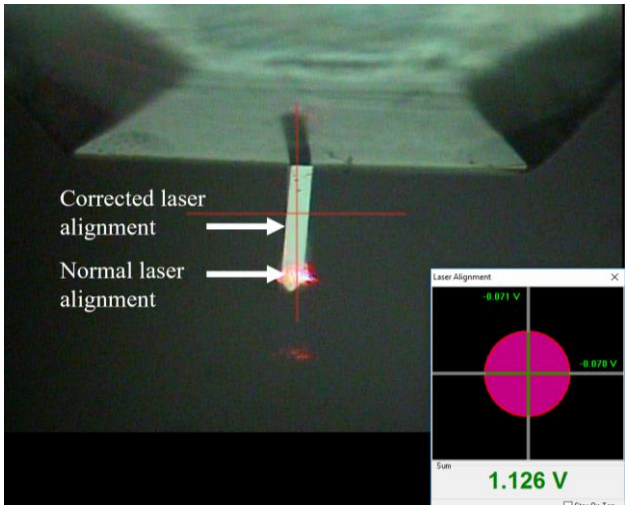

Figure 36: Image of the corrected laser alignment to minimize the oscillating motion of the colloidal probe when approaching and retracting from the surface. Normally, the laser is aligned at the base of the apex of the cantilever.

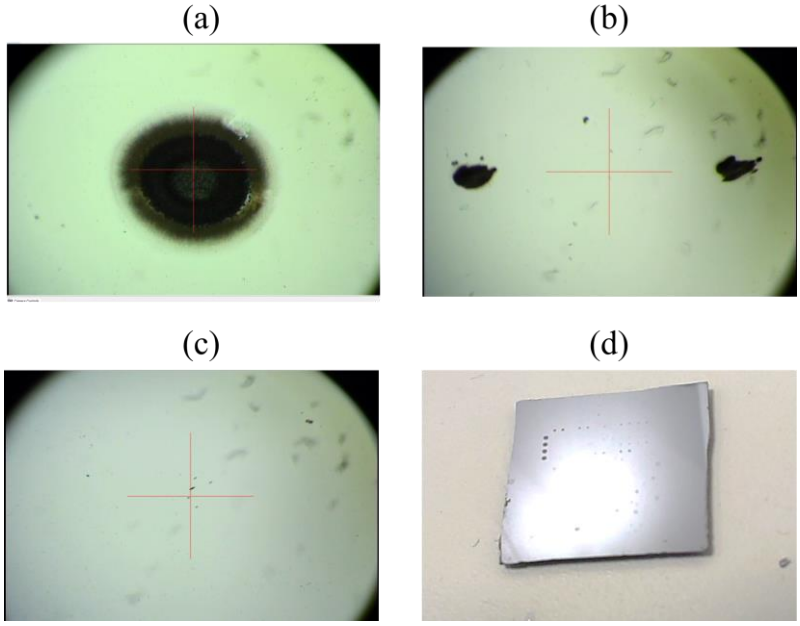

Figure 37: Images of the laser-ablated spots. (a) shows the identifier spot, (b) shows a spot at 40 mW at a relatively long exposure time, (c) shows a barely visible spot at a relatively short exposure time, and (d) shows the laser-ablated wafer in its entirety.

Appendix III: Equipment Specifications

Innova Specifications

Sample Size	45 mm x 45 mm x 18 mm
Motorized Z Travel	18 mm, with pitch and tilt capability
Closed-Loop, Large-Area Scanner	XY >90 µm, Z >7.5 µm
Open-Loop, Small-Area Scanner	XY >5 µm, Z >1.5 µm
Z Noise Floor	<50 pm RMS, typical imaging bandwidth
Closed-Loop XY Noise	<1.2 nm RMS, typical imaging bandwidth
Z Linearizer Noise	<200 pm RMS, typical imaging bandwidth
Open-Loop XY Drift	<1 nm/min
Closed-Loop WY Drift	<3 nm/min
Open-Loop Warm-Up Time	15 min
Electronics	20-bit DAC scan control, 8 ADCs (100 kHz ±10V); Digital force and position feedback, programmable/controllable via external signals; Integrated software-configurable signal access and routing; 2 full-digital lock-ins
Optics	On-axis, 1.25 mm - 0.25 mm FOV; Software-controlled 5x motorized zoom; 10x objective (50x optional); <2 µm resolution (0.75 µm resolution with 50x)
System Software	NanoDrive real-time control and NanoScope Analysis included
AFM Modes	Standard: Contact Mode, TappingMode, PhaseImaging, LiftMode, Magnetic Force Microscopy (MFM), Electrostatic Force Microscopy (EFM), Dark Lift, Lateral Force Microscopy, Nano-Indentation, Force Spectroscopy Optional: Scanning Tunneling Microscopy (STM), Low-Current Scanning Tunneling Microscopy (LC-STM), Force Modulation Microscopy (FMM), Piezo Response Microscopy, Electrochemical Scanning Probe Microscopy (ECSPM), Single- and dual-pass Kelvin Probe Force Microscopy (KPFM), Conductive Atomic Force Microscopy (CAFM), Scanning Capacitance Microscopy (SCM), Nanolithography, Nano Thermal Analysis (VITA)
Weights and Measures	Microscope: 14" H x 14" W x 10" D (35.5 cm x 35.5 cm x 25.5 cm); 26.5 lb (12 kg); Add 4" (10 cm) in rear for cables Controller: 23" H x 13.5" W x 21" D (58.5 cm x 34.5 cm x 53.5 cm); 73 lb (33 kg); Add 4" (10 cm) in rear for cables
EH&S Compliance	CE

Figure 38: Specifications of the Innova. [31]

UMT TriboLab Specifications

Measurement Capability	Universal mechanical and tribology testing
System Attributes	Integrated high-speed/high-torque drive motor; Servo-controlled, precision Z-axis load stage; Motorized positioning "lateral" stage; Tool-less lower drive retaining system; 8 data channels (expandable to 16 channels), 16-bit DAS up to 200 kHz; Auto-recognition Tribo ID technology; Built-in temperature controller
Software	TriboScript tribology scripting software; Viewer data analysis package
Computer System	64-bit Professional PC with MS Windows OS, 16GB SDRAM, 500GB HDD, wireless keyboard and mouse
Vertical Travel	Distance: 150 mm; Encoder resolution: 0.5 µm; Speed: 0.002 to 10 mm/s
Lateral Travel	Distance: 120 mm; Encoder resolution: 0.25 µm; Speed: 0.002 to 10 mm/s
Load Range	1 mN to 2,000 N
Torque Capability	5 Nm @ 100 rpm, 2.5 Nm @ 5,000 rpm
Temperature Control	-25°C to 1000°C
Power Requirement	220VAC, 8kW recommended
Footprint	W: 15.5" x D: 24" x H: 30.5"
Optional Features	
Humidity Control	5% to 85% RH
Optical Microscope	5X, 10X, 25X optical objectives; 1280 x 1024 digital camera
Linear Stage	Speed: 0.002 mm/s to 10 mm/s; Position resolution: 1 µm; Max. travel: 120 mm
Rotary Stage	Speed: 0.1 to 5,000 rpm
Reciprocating Stage	Speed: 0.1 to 60 Hz
Block-on-Ring Stage	Speed: 0.1 to 5,000 rpm
Acoustic Emmision	Frequency response: 0.2 to 5 MHz
Electrical Contact Resistance	5 mOhm to 1 MOhm
Power Supply	Current Range: ±1µA up to ±1A; Resolution: 10nA; Voltage Range: ±200mV up to ±10V; Resolution 6.1µV
Programmable Pump	Flow rate: 2.2 to 480 mL/min

Figure 39: Specifications of the UMT TriboLab. [32]

Appendix IV: Python Script

```
import matplotlib.pyplot as plt;
import numpy as np;
subscript = str.maketrans("0123456789", "₀₁₂₃₄₅₆₇₈₉")  #For subscript in string

############### General settings for plotting figures ##########################
plt.rc('font', size=16);
plt.rc('axes', titlesize=18);
plt.rc('axes', labelsize=20);
plt.rcParams['axes.labelpad'] = 10.0
plt.rcParams['xtick.major.pad']='8'
plt.rcParams['ytick.major.pad']='8'
plt.rcParams["font.family"] = "serif"
plt.rcParams['axes.titlepad'] = 30
#plt.rcParams['axes.formatter.use_locale'] = True
save_results_to = \
    ('D:/ARCNL Surfdrive/Verslaglegging/Figuren/Capillary forces/')
dpi = 500

print("\n===== Cappilary Force as a function of seperation distance h ======")
############### All the variables and equations ##########################
F = 3                   #--Variable-- 0=m 3=mm 6=um 9=nm
Factor_1 = 10**-F       #Scale Factor
γ = 72.75*10**-3        #Water surface tension
θ = 110     /180*np.pi  #--Variable-- Contact angle
r = 10*Factor_1         #--Variable-- Radius of spherical droplet


V = (4/3)*np.pi*r**3    #Volume of sphere
V_string = np.around((V*(1000)**F), decimals = 4)
h_min = r/1000   #--Variable-- Mininum distance
h_max = r/10       #--Variable-- Maximum disctance
steps = 100000    #Number of steps

h = np.linspace(h_min, h_max, steps)       #Height variation
R = np.array(np.sqrt(V/(np.pi*h)))         #Wetted radius
r_1 = R+((h*(1-np.sin(θ)))/(-2*np.cos(θ)))  #Radius r_1
r_2 = h/(-2*np.cos(θ))                  #Radius r_1

if Factor_1 == 10**-0: #Value in standard-range
    Sc_1 = ""
if Factor_1 == 10**-3: #Value in milli-range
    Sc_1 = "m"
if Factor_1 == 10**-6: #Value in micro-range
    Sc_1 = "μ"
if Factor_1 == 10**-9: #Value in nano-range
    Sc_1 = "n"
```

```
47.
48. F_ten = -np.sqrt((4*np.pi*V)/h)*γ*np.sin(θ)
49. F_lap = (V*γ/h)*((1/((np.sqrt(V/(np.pi*h)))+((h*(1-np.sin(θ)))\
50.         /(-2*np.cos(θ)))))+(1/(h/(-2*np.cos(θ)))))
51. F_cap = np.array(F_ten + F_lap )
52.
53. def Diff_sum_data(h, F_cap):
54.     '''
55.         Calculates the stiffness k
56.         Arguments:
57.         h: array with separation distance values
58.         F_cap: array with capillary force values
59.         Returns:
60.         The stiffness k [N/M]
61.     '''
62.     F_cap_diff = 0
63.     F_cap_diff_array = []
64.     for i in range(1, len(h)):
65.         F_cap_diff = ((F_cap[i]-F_cap[i-1])/(h[i]-h[i-1]))
66.         F_cap_diff_array.append(F_cap_diff)
67.     return F_cap_diff_array
68.
69. Stiffness = np.abs(Diff_sum_data(h, F_cap))
70. Stiffness_max = np.max(Stiffness) #The maximum value of stiffness in array
71. Grad_func = np.abs(np.gradient(F_cap, h[1]-h[0])) #--> Used as a check
72.
73. print("\nVolume:    ", V_string, "{}m^3".format(Sc_1))
74. No_array = 5            #For printing first No. elements in array
75. print("\n*Array shows only the first" + " {} ".format(No_array) + "elements*")
76. print("\nHeight" + " ({}m)".format(Sc_1) + ":\n", h[:No_array]/Factor_1)
77. print("\nWetted Radius R" + " ({}m)".format(Sc_1)\
78.       + ":\n", R[:No_array]/Factor_1)
79. print("\nRadius r1".translate(subscript) + " ({}m)".format(Sc_1)\
80.       + ":\n", r_1[:No_array]/Factor_1)
81. print("\nRadius r2".translate(subscript) + " ({}m)".format(Sc_1)\
82.       + ":\n", r_2[:No_array]/Factor_1)
83. print("\nTension force (N) \n", F_ten[:No_array])
84. print("\nLaplace force (N)\n", F_lap[:No_array])
85. print("\nCapillary force (N)\n", F_cap[:No_array])
86.
87. plt.figure(figsize=(6,6));
88. #plt.title(" Radii $\itR$ and $\itr_1$ with respect to height $\ith$" \
89. #         + "\n Water Volume = {}".format(V_string) + "{}m\xB3".format(Sc_1))
90. plt.ylabel("Radii " +"({}m)".format(Sc_1));
91. plt.xlabel("Height $\it{h}$ " + "({}m)".format(Sc_1));
92. plt.ylim(0, (Max_Val_1/Factor_1))
93. plt.plot(h/Factor_1, R/Factor_1, color = "mediumblue")
94. plt.plot(h/Factor_1, r_1/Factor_1, color = "Firebrick")
```

```
plt.gca().legend(("R", "$r_1$"), title = "radii",fancybox=True, framealpha=1)
plt.show();

plt.figure(figsize=(6,6));
#plt.title(" Radii $\itr_2$ with respect to height $\ith$" \
#         + "\n Water Volume = {}".format(V_string) + " {}m\xB3".format(Sc_1))
        plt.ylabel("Radius $\it{r_2}$ " +"({}m)".format(Sc_1));
        plt.xlabel("Height $\it{h}$ " + "({}m)".format(Sc_1));
        plt.plot(h/Factor_1, r_2/Factor_1, color = "green")
        plt.gca().legend(("$r_2$", ""), title = "radii",fancybox=True, framealpha=1)
        plt.show();

        customxtick = [0.0, 0.2, 0.4, 0.6, 0.8, 1]

        plt.figure(figsize=(6,6));
        #plt.title("Force ${\itF_L}$ with respect height ${h}$")
        plt.ylabel("Force $\it{F_{Lap}}$ (N)");
        plt.xlabel("Seperation distance $\it{h}$ " + "({}m)".format(Sc_1));
        plt.plot(h/Factor_1, F_lap, color = "k")
        plt.xlim(0, h_max)
        plt.ylim(0, 50)
        plt.xticks(customxtick)
        plt.savefig(save_results_to + 'Example F_Lap', dpi = dpi, bbox_inches="tight")
        plt.show();

        plt.figure(figsize=(6,6));
        #plt.title("Forces ${\itF_t}$ with respect height ${h}$")
        plt.ylabel("Force $\itF_{ten}$ (N)");
        plt.xlabel("Seperation distance $\it{h}$ " + "({}m)".format(Sc_1));
        plt.plot(h/Factor_1, F_ten, color ="k")
        plt.xlim(0, h_max)
        plt.ylim(-0.07, 0)
        plt.xticks(customxtick)
        plt.savefig(save_results_to + 'Example F_ten', dpi = dpi, bbox_inches="tight")
        plt.show();

        plt.figure(figsize=(6,6));
        #plt.title("Force ${\itF_C}$ with respect height ${h}$")
        plt.ylabel("Force $\it{F_{cap}}$ (N)");
        plt.xlabel("Seperation distance $\it{h}$ " + "({}m)".format(Sc_1));
        plt.plot(h/Factor_1, F_cap, color = "k")
        plt.xlim(0, h_max)
        plt.ylim(0, 50)
        plt.xticks(customxtick)
        plt.savefig(save_results_to + 'Example F_cap', dpi = dpi, bbox_inches="tight")
        plt.show();

        Ratio_lap = (F_lap)/(F_lap+np.abs(F_ten))
```

```
143.        Ratio_ten = (np.abs(F_ten))/(F_lap+np.abs(F_ten))
144.
145.        plt.figure(figsize=(6,6));
146.        #plt.title("Normalized Ratio F_lap/F_ten$")
147.        plt.ylabel("Normalized Force (N)");
148.        plt.xlabel("Seperation distance $\it{h}$ " + "({}m)".format(Sc_1));
149.        plt.plot(h/Factor_1, Ratio_lap, color = "k")
150.        plt.plot(h/Factor_1, Ratio_ten, color = "k" , linestyle = '--')
151.        plt.xlim(0, h_max)
152.        #plt.ylim(0, 1)
153.        plt.xticks(customxtick)
154.        plt.gca().legend(("$\it{F_{Lap,N}}$" , "$\it{F_{ten,N}}$"),\
155.            fancybox=True, framealpha=1, fontsize='20')
156.        plt.savefig(save_results_to + 'Normalized Ratio', dpi = dpi,\
157.            bbox_inches="tight")
158.        plt.show();
159.
160.        plt.figure(figsize=(6,6));
161.        #plt.title("Stiffness ${\itk}$ with respect height ${h}$")
162.        plt.ylabel("Stiffness $\it{k}$ (N/m)");
163.        plt.xlabel("Height $\it{h}$ " + "({}m)".format(Sc_1));
164.        plt.yscale("log")
165.        plt.plot(h[0:(len(h)-1)]/Factor_1, Stiffness, color = "k")
166.        #plt.plot(h/Factor_1, Grad_func, color = "green")
167.        plt.show();
168.
169.        ################ Test For specific values#####################
170.        print("\n############## Compressed state ##############")
171.        print("h =", h[-1]/Factor_1, "{}m".format(Sc_1))
172.        print("R =", R[-1]/Factor_1, "{}m".format(Sc_1))
173.        print("F_ten" ,F_ten[-1])
174.        print("F_Lap" ,F_lap[-1])
175.        print("F_cap" ,F_cap[-1])
176.
177.        print("\n############## Uncompressed state ##############")
178.        print("h =", h[0]/Factor_1, "{}m".format(Sc_1))
179.        print("R =", R[0]/Factor_1, "{}m".format(Sc_1))
180.        print("F_ten" ,F_ten[0])
181.        print("F_Lap" ,F_lap[0])
182.        print("F_cap" ,F_cap[0])
```